Hadron-Nucleus Scattering

by

Li, To-Sing

A Thesis Submitted In Partial Fulfillment
of the Requirements for the Degree of
Master of Philosophy in Physics

The Chinese University of Hong Kong

May 1986

Table of Contents

Acknowledgement

I would like to express my sincere gratitude towards my supervisor, Dr. Kenneth Young, for his patience and brilliant guidance during my work and the preparation of this thesis.

Abstract

The basic experimental data and theoretical ideas about high energy hadron-hadron and hadron-nucleus collisions are reviewed. Special attention is paid to the single-particle distribution. Based on the concept of partition temperature, we proposed a model to describe the pseudo-rapidity distribution in hadron-nucleus scattering. And the parameters of the model can be summarised in simple phenomenological rules.

Chapter 1

Introduction

1.1 Overview

High energy physics studies the ultimate constituents of matter and the nature of the interactions between them. Experimental research is performed with large particle accelerators and their associated detection systems. High energies are necessary for two reasons; firstly we wish to investigate very small scales of distance associated with the elementary constituents; secondly many fundamental constituents have large masses and require correspondingly high energies for their creation and study. This thesis is organised as follow. The rest of this chapter gives a brief review of the main tools in experimental high energy physics. Chapter 2 summarizes some basic experimental data and theoretical ideas about hadron-hadron collisions. Chapter 3 reviews the background and in Chapter 4 we present our own work on hadron-nucleus scattering. Chapter 5 will be the conclusion of the thesis.

1.2 Energy parameter s

The energy parameter of interest is the total energy in the centre of mass, for this is the energy available

for the production of particles, and a measure of the violence of the collision. It is believed that more violent collisions may be better probes of the fundamental nature of elementary particles and strong interactions. It has been conventional to describe the total centre of mass energy by its square, usually denoted by s. If two particles A and B of four momenta P_a and P_b collide, we have

$$s = (P_a + P_b)^2$$
$$\equiv (P_a + P_a)_\mu (P_a + P_a)^\mu .$$

It is obvious that s is Lorentz invariant.

1.3 Accelerators

1.3.1 Conventional Accelerator

The vast bulk of present experimental knowledge in the high energy field has been obtained with proton and electron accelerators in which the beam has been extracted and directed onto an external target --- the so-called fixed-target experiments. High-energy proton accelerators can also be used to provide intense secondary beams of hadrons ($\pi^{\pm}$, $K^{\pm}$, p, $\bar{p}$) and leptons ($\mu^{\pm}$, ν). As an example, Fig. 1.3.1 shows the general layout of the secondary beam lines around the 500 GeV proton synchrotron at Fermilab. The 2.5 km long beam to the neutrino area provides beams of muons as well as neutrinos. If we denote the beam particle by A which has mass M_a and laboratory

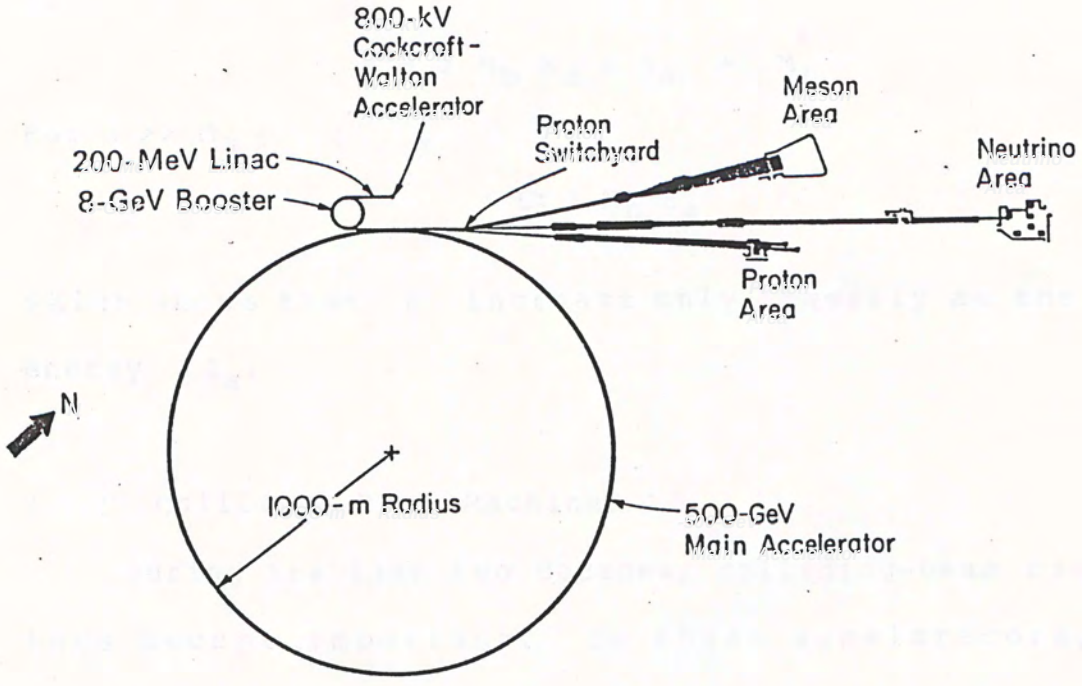

Fig. 1.3.1 Layout of the 500 GeV proton synchrotron and beam lines at Fermilab. Taken from Perkins (1982).

energy E_a and the stationary target particle B has mass M_b, we have:

$$P_a = (E_a; P_x, P_y, P_z)$$

$$P_b = (M_b; 0, 0, 0)$$

so

$$s = 2 M_b E_a + M_a^2 + M_b^2$$

For $s >> M_a$

$$s \simeq 2 M_b E_a$$

which shows that s increase only linearly as the beam energy E_a.

1.3.2 Colliding Beam Machines

During the last two decades, colliding-beam machines have become important. In these accelerators, two counter-rotating beams of particles collide in several interaction regions around the ring. Fig. 1.3.2 shows the layout of the accelerator complex at CERN. The advantage is obvious in terms of the large centre of mass energy available. If two beams of energy E circulate in opposite directions in a storage ring, then in a head - on collision s is given by

$$s = 4 E^2$$

Thus high s can be achieved with much lower beam energies. For illustration, Table 1.3.1 lists the existing

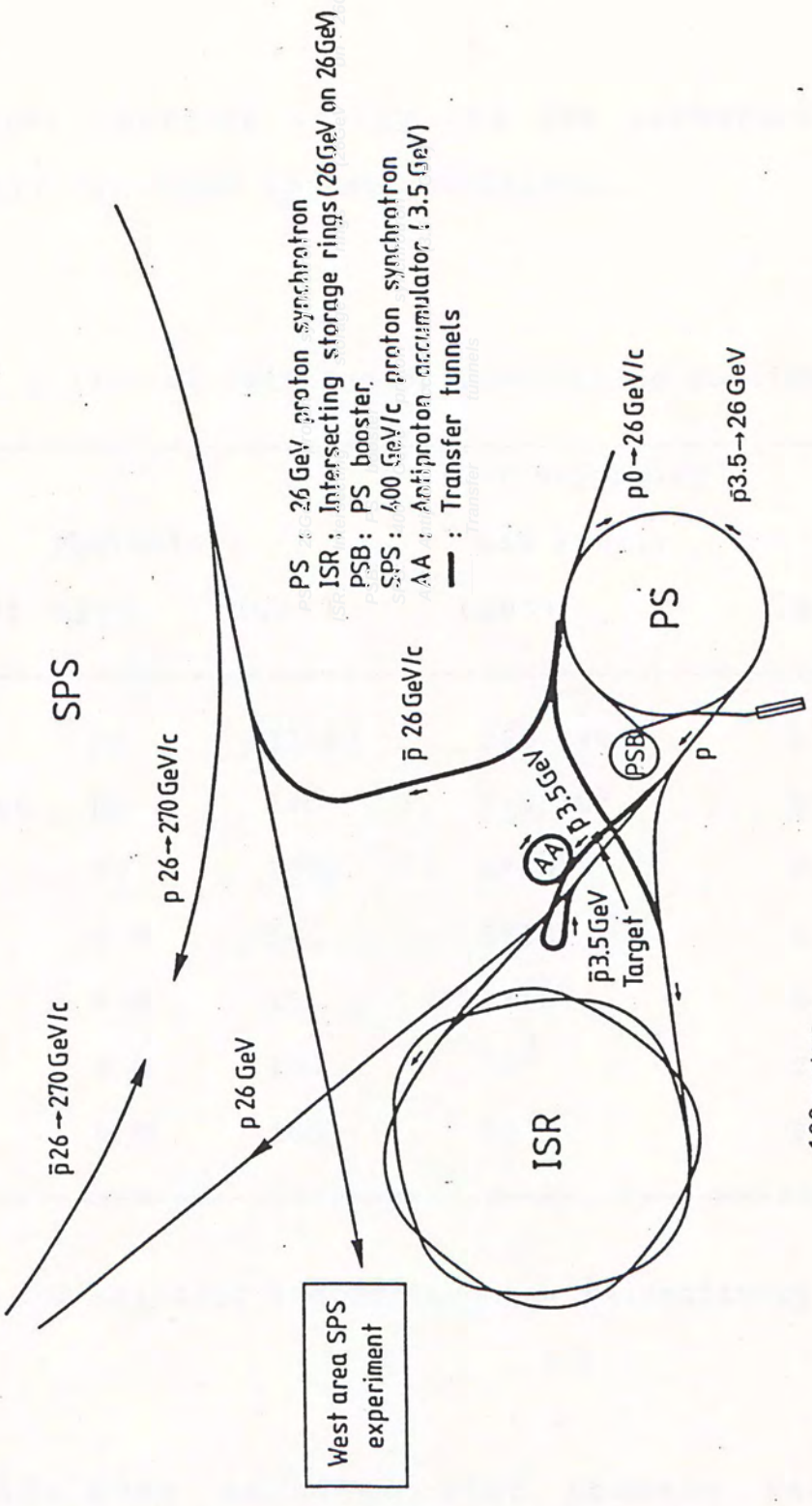

Fig. 1.3.2 Layout of the accelerator complex at CERN. Taken from Perkins (1982).

or forthcoming collider energy and the corresponding incident energy for fixed target accelerator.

Table 1.3.1 A list of existing or forthcoming colliders

Accelerator	particle type	(GeV)	Corresponding Lab Energy (GeV)	Status
ISR	pp	23-63	260-1985	E*
CERN Collider	pp	540	$1.5*10^5$	E
Tevatron	pp	2000	$2*10^6$	F
CESR	e e	14	$2*10^5$	E
PETRA	e e	15	$2*10^5$	E
SLC	e e	100	10^7	E
LEP	e e	100	10^7	F

* E, F stand for existing and forthcoming respectively

Colliding-beam machines also possess severe disadvantages. The colliding particles must be stable. All colliders so far built or planned are only of the pp, e^+e^-, $p\bar{p}$ or ep variety. Secondly, the collision rate in the intersection region is low. The interaction rate can be written as

$$\frac{dn}{dt} = L\sigma$$

where L is the luminosity and σ is the cross-section. For example, the maximum luminosity for the ISR is only 10^{32} $cm^{-2}s^{-1}$ with an incident beam of $2*10^{12}$ protons/sec. For the same incident beam rate, the luminosity for a typical liquid-hydrogen target 1 m long is 10^{37} cm^{-2} s^{-1} .

1.4 Detectors

Nowadays, the detection of a particle means much more than its mere localization in space. It is also required to record its energy and momentum , arrival time and the identity. A number of tasks have to be performed in order to extract the necessary information, for example :

(1) the charged-particle trajectories have to be localized in space, i.e. their space coordinates and directions have to be measured;

(2) to measure charge and momentum, the curvature of each trajectory in a magnetic field has to be determined;

(3) a simultaneous measurement of momentum and velocity (by time-of-flight or Cerenkov radiation), determines the particle mass.

Dead time, space, time and energy resolution are

important parameters for detectors. Typical numbers for different detectors are given in Table 1.4.1 .

Table 1.4.1 Detector Parameters

Detector	Time resolution, sec	Dead time, sec	Space resolution, cm	Volume, cm^3
Ionization chamber	10^{-3}	10^{-2}	(a)	$1-10^5$
Geiger–Müller counter	10^{-6}	10^{-4}	(a)	$1-10^4$
Semiconductor counter	10^{-8}	10^{-6}	0.5	0.1
Scintillation counter	10^{-8}	10^{-6}	(a)	$1-10^4$
Cerenkov counter	10^{-9}	10^{-8}	(a)	$10-10^4$
Photographic emulsion			10^{-4}	10^3
Cloud chamber	10^{-2}	100	0.05	10^5
Bubble chamber	10^{-3}	1	5×10^{-3}	10^5
Spark chamber	10^{-6}	10^{-2}	0.05	5×10^5

[a] Depends on the size of the instrument.

(Taken from Segre, 1973)

1.4.1 Bubble Chamber

For more than 20 years the bubble chamber has been an important tool for studying multiparticle events. Complete track reconstruction and efficient particle identification is possible. During the past years, the use of the bubble chamber has diminished because of the following reasons.

(1) it cannot be used as a selective, triggerable detector,

(2) it has a low repetition rate (1 - 10 per

second);

(3) the reconstruction time of events from the film is slow, 10^5 events per year on automatic measuring devices.

1.4.2 Multiwire Proportional Counter

Multiwire proportional counter (MWPC) was invented by Charpak (1968, 1970). This device consists of many parallel anode wires stretched in a plane between two cathode planes (Fig. 1.4.1). The different anode wires act as independent detectors. The effective spatial resolution is of the order 1 mm.

1.4.3 Streamer Chambers

When a short high-voltage pulse (typically 10 - 50 kV/cm during 5 - 20 ns) is applied across a flat electrode structure (Fig. 1.4.2), electric breakdown of the gas will occur. And it can grow into the so-called streamer mode. Based on this effect, the streamer chamber was developed by Chikovani et al. (1964). It has space resolution and vertex reconstruction capabilities similar to those of the bubble chamber. An advantage over the bubble chamber is that it is triggerable and comparably fast.

Today, streamer chambers are frequently used as vertex detectors. Fig. 1.4.3 shows the recording of a high-energy interaction from a CERN experiment. It demonstrates the excellent quality of multitrack recording

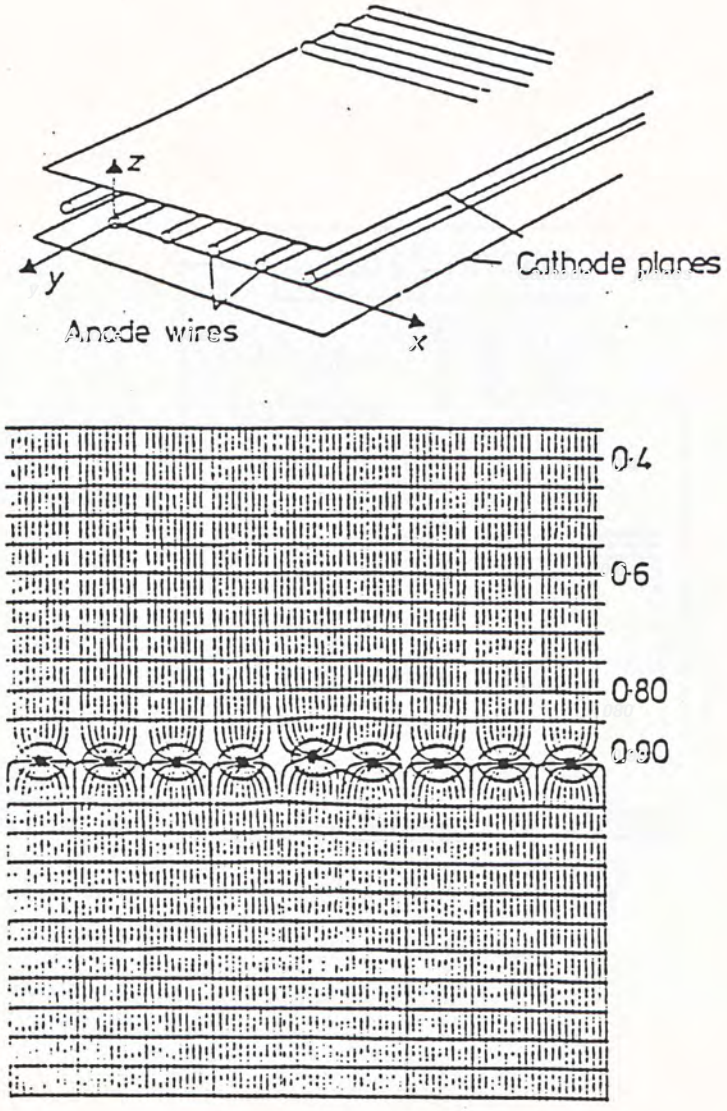

Fig. 1.4.1 Basic structure of an MWPC. Taken from Fabjan (1980).

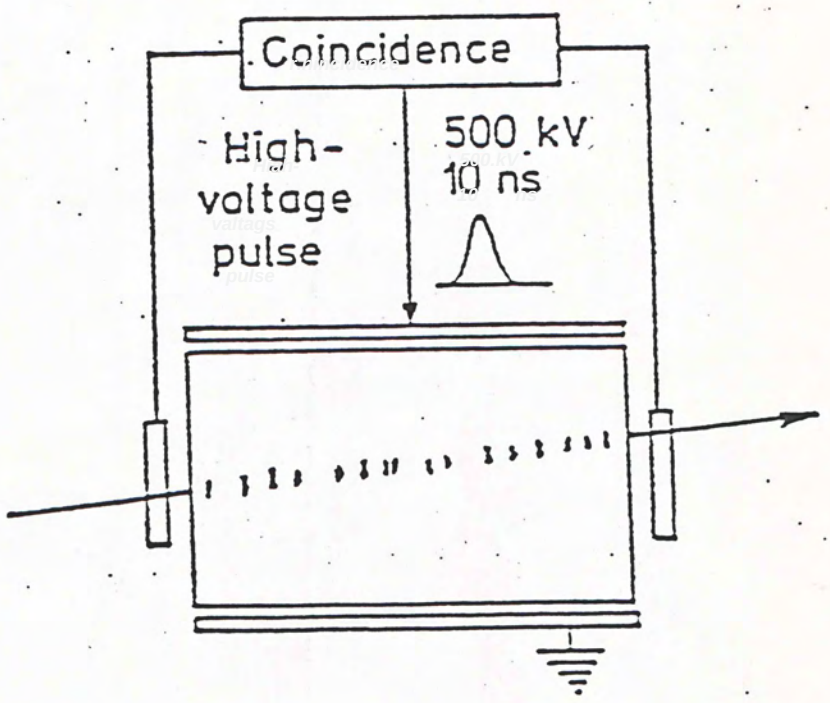

Fig. 1.4.2 Basic structure of a streamer chamber.
Taken from Fabjan (1980).

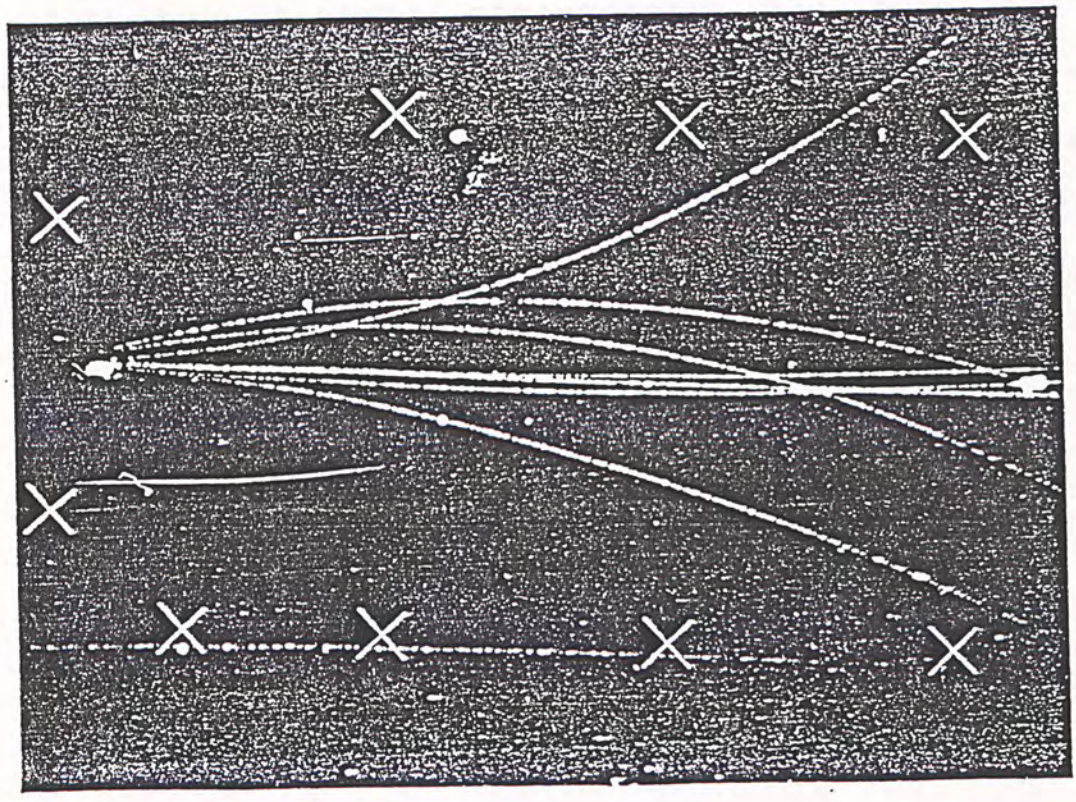

Fig. 1.4.3 Multitrack event from NA5 streamer chamber experiment at CERN. Taken from Fabjan (1980).

that can be obtained.

1.4.4 Nuclear Emulsions

Nuclear emulsion used for radiation detection consists of silver halide microcrystals or grains. An ionizing particle passing through in the emulsion will reduce some of the silver halide molecules in the same way as photons do in normal photography. The advantages of nuclear emulsions are simplicity, ability to record the path of a particle, large recording range (from very low to almost unlimited flux), and the ability to remember. The disadvantages are delay in getting the information and impossibility of coincidence measurements.

Chapter 2

Hadron-Hadron Collisions

2.1 Introduction

In this chapter we summarize some of the more basic and well-known properties of hadron-hadron collisions.

2.2 Total Cross-Section

The s dependence of the total cross-section σ_{tot} of pp collision is shown in Fig. 2.2.1. Generally speaking, the energy dependence is very complicated at low energy, including resonance peaks. At high energies (above 1 Gev) the curve becomes smooth and increases slowly as $(\ln s)^2$.

2.3 Elastic and Inelastic Cross-Sections

An important type of scattering is elastic scattering, i.e. scattering during which the quantum numbers of the scatterer and the target do not change, and there is no energy transfer to the internal degrees of freedom. The datas (Fig. 2.2.1) shows that σ_{el} grows logarithmically with s. An interesting result is that at ISR (s ranges from 23 - 63 Gev), the ratio of $\sigma_{el} / \sigma_{tot}$ is apparantly constant at 0.18 (Thomé et al., 1977). But recent data from CERN Collider shows that at 540 Gev the elastic cross-section for $p-\bar{p}$ increases to 13 mb (Battiston et al., 1982), i.e. about 0.21 of σ_{tot} .

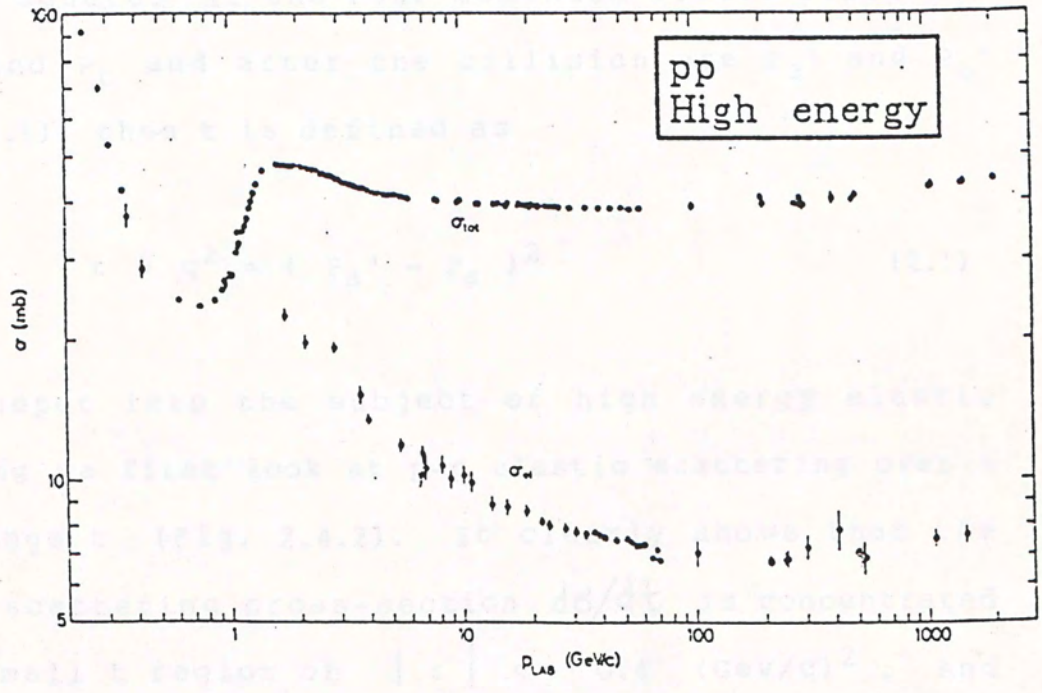

Fig. 2.2.1 Total and elastic p-p cross-section data.
Taken from Barash-Schmidt (1980).

2.4 Elastic Scattering And The Diffraction Peak

In elastic scattering it is conveinent to use a Lorentz invariant parameter t, called the four momentum transfer square. If the four momentum before collision are P_a and P_b and after the collision are P_a' and P_b' (Fig. 2.4.1), then t is defined as

$$t = q^2 = (P_a' - P_a)^2 \qquad (2.1)$$

To go deeper into the subject of high energy elastic scattering we first look at p-p elastic scattering over a large range t (Fig. 2.4.2). It clearly shows that the elastic scattering cross-section $d\sigma/dt$ is concentrated in the small t region of $|t| < 0.4$ $(Gev/c)^2$. And $d\sigma/dt$ decreases exponentially with $|t|$, it is customary to fit this region with the form

$$\frac{d\sigma}{dt} = A(s)\, e^{-b(s)|t|} \qquad (2.2)$$

At high energies the slope parameter b is in the range of 5 to 13 $(Gev/c)^{-2}$. Fig. 2.4.3 (Predazzi, 1979) shows the variation of b versus s. It is important to note that the strong small t peak is evident at all the energy presented, and the shape of that peak changes very little with energy.

Finally, to look at some very different systems, in

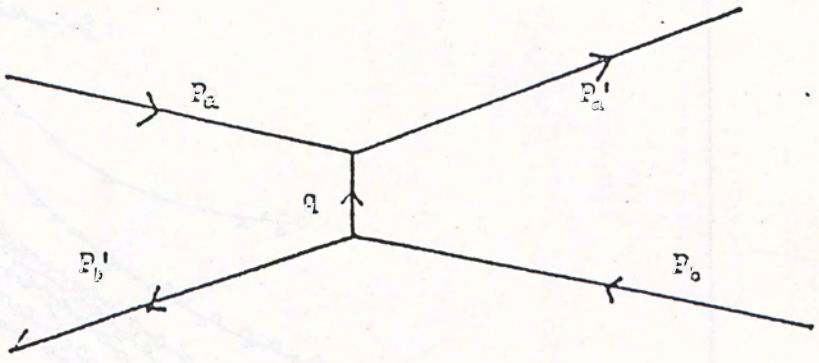

Fig. 2.4.1 Kinematics of elastic scattering.

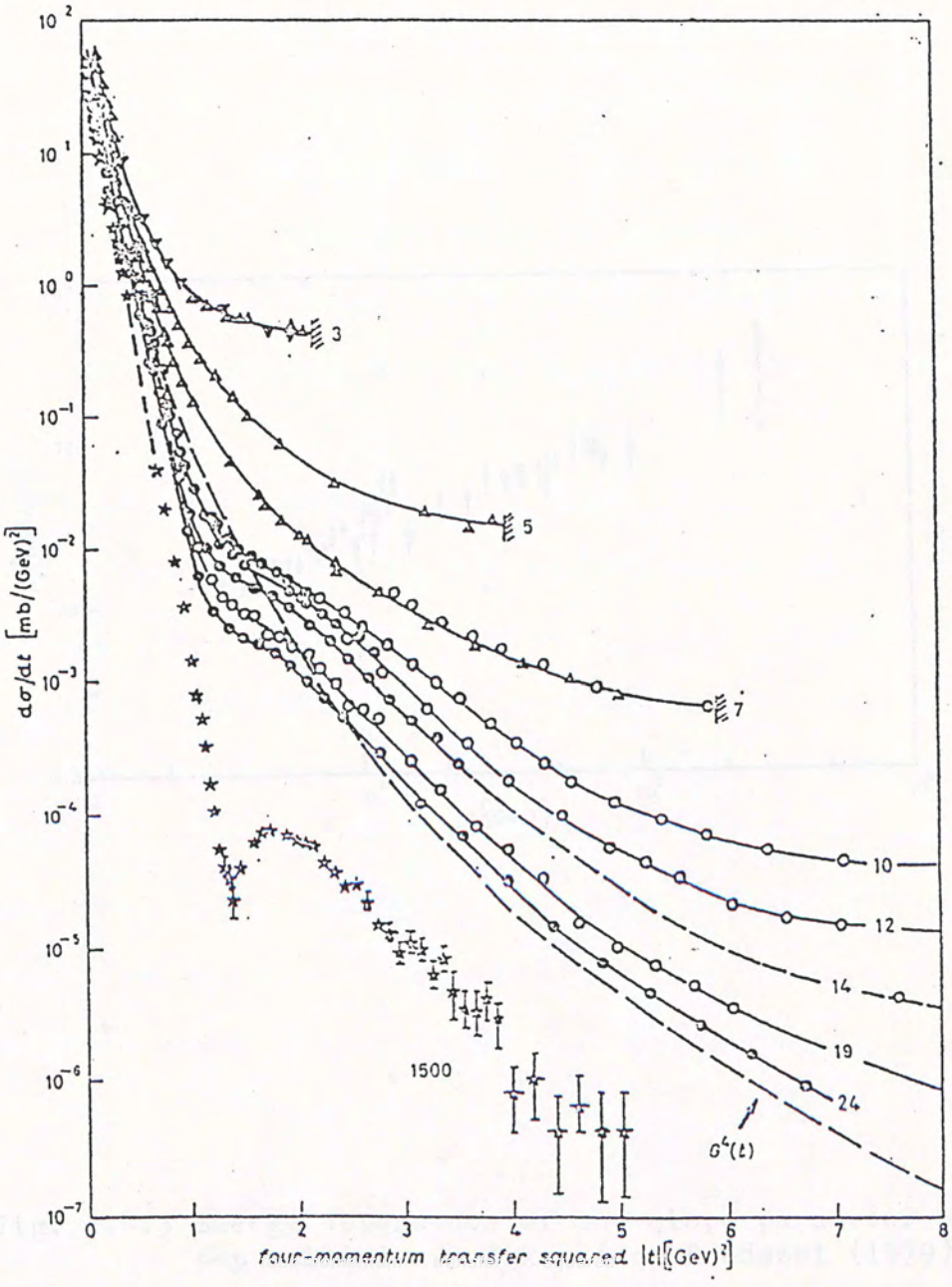

Fig. 2.4.2 Elastic differential cross-section for p-p collisions at various energies. Taken from Predazzi (1979).

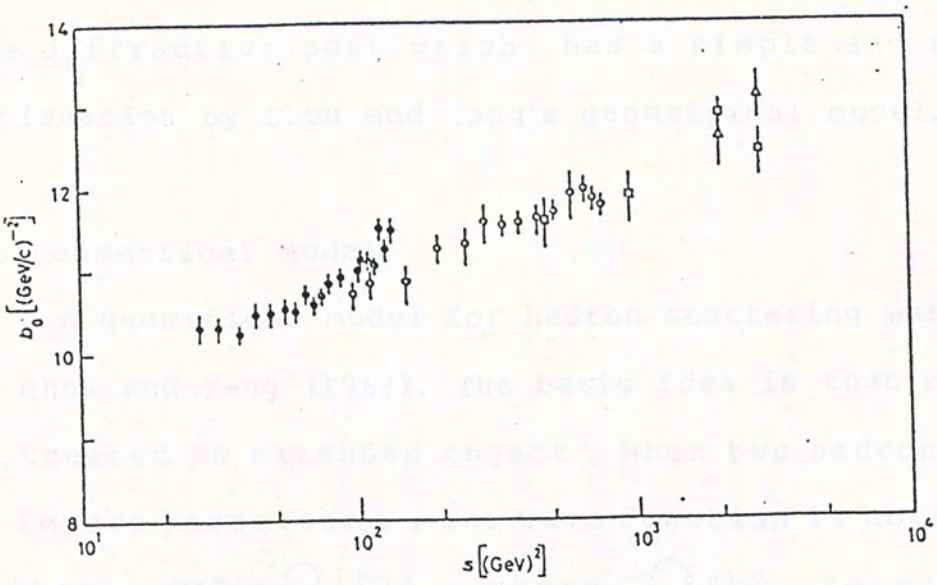

Fig. 2.4.3 Energy dependence of the slope parameter b for p-p collision. Taken from Predazzi (1979).

Fig. 2.4.4 we present the elastic scattering of π^- meson on proton (Giacomelli, 1972) and photon on proton (Anderson, 1970). In all these systems the high energy elastic differential cross-section is dominated by a forward peak. This small t peak, a universal property of all hadron-hadron systems, is ascribed to a very general process --- diffraction elastic scattering. It is called the diffractive peak which has a simple and beautiful explanation by Chou and Yang's geometrical model.

2.5 Geometrical Model

A geometical model for hadron scattering was proposed by Chou and Yang (1968). The basic idea is that hadron can be treated as extended object . When two hadrons collide at impact parameter b , the wave function is absorbed by a factor $\exp(-\Omega(b))$, where $\Omega(b)$ is called the blackness , a measure for absorption. Therefore the scattered wave for the elastic case is $1 - \exp(-\Omega(b))$. The scattering amplitude is then found to be

$$f(\theta,\phi) \simeq \frac{ik}{2\pi} \int e^{i\bar{q}\cdot\bar{b}} (1-e^{-\Omega}) d^2b \qquad (2.3)$$

$\bar{q}$ is the four-momentum transfer defined in Eq. (2.1)

Eq. (2.3) is the so-called eikonal approximation. Therefore the differential cross-section is written as

> Missing eqn.

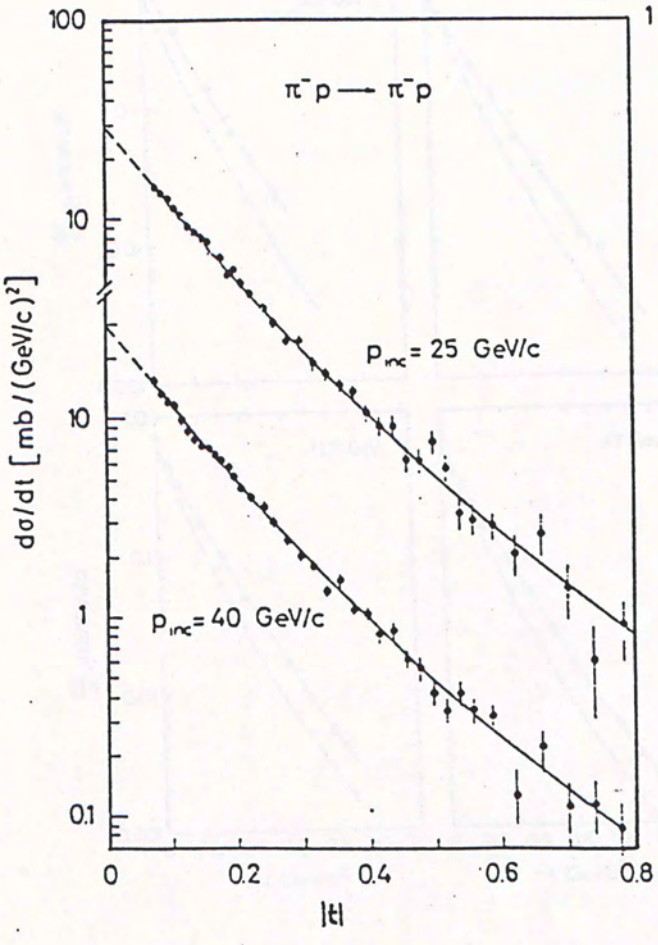

Fig. 2.4.4a Elastic differential cross-section for $\pi^- p$ scattering at 25 GeV/c. Taken from Giacomelli (1972).

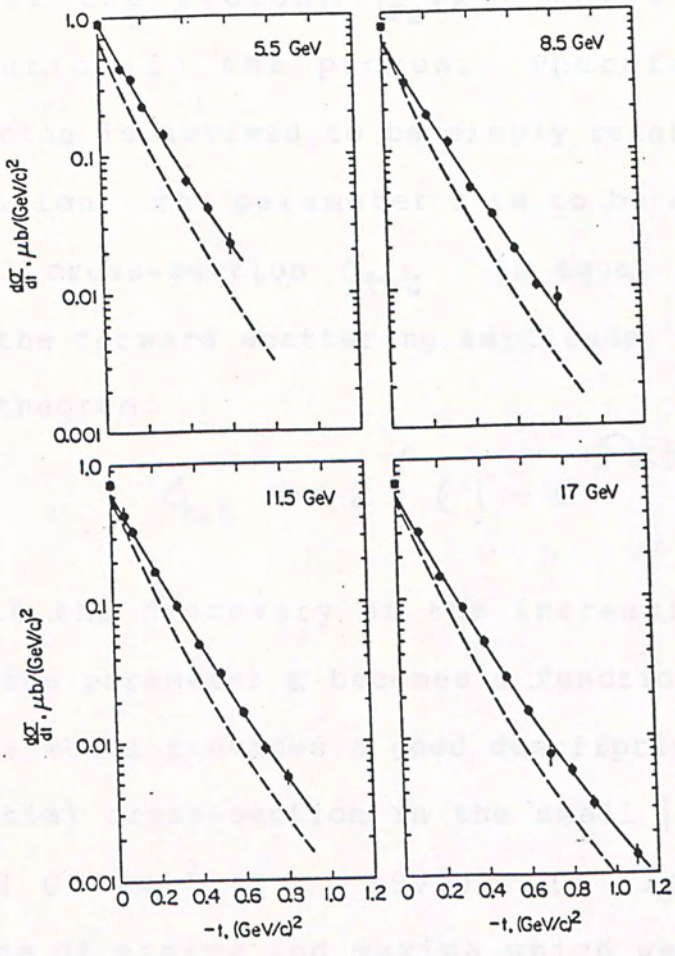

Fig. 2.4.4b The photon-proton elastic differential cross-section. Taken from Anderson (1970).

In addition, $\Omega(b)$ is related to the matter distribution inside the particle. In p-p scattering, $\tilde{\Omega}(k)$ is written as $K G_E(k)$, where $\tilde{\Omega}(k)$ is the two-dimensional Fourier transform of $\Omega(b)$ and $G_E(k)$ is the electric form factor of the proton. $G_E(k)$ tells us the charge distribution in the proton. Therefore the matter distribution is assumed to be simply related to the charge distribution. The parameter K is to be adjusted so that the total cross-section σ_{tot} is equal to the imaginary part of the forward scattering amplitude, as the result of optical theorem:

$$\sigma_{tot} = 2 \int (1 - e^{-\Omega(b)}) \, d^2b$$

With the discovery of the increasing total cross-section the parameter K becomes a function of energy K(s).

This model provides a good description of the elastic differential cross-section in the small $|t|$ region, $|t| < 1.2$ (Gev/c)^2 (Kac, 1973). It also predicts the existence of minima and maxima which were found in CERN experiments (Böhm et al., 1974). So we can conclude that the geometrical aspects in hadron scattering are well supported by experiments.

2.6 General Feature Of Inelastic Interaction

2.6.1 Multiplicity

We are concerned with reactions like:

$$A + B \longrightarrow C_1 + C_2 + \ldots + C_n \qquad (2.4)$$

where A, B, C_1, C_2, ... , C_n are stable or metastable hadrons (mean life >> 10^{-22} s), e.g. p, π, K, ... The number n is called multiplicity.

In usual detection systems such as bubble chambers, spark chambers and scintillation counter systems, it is easy to observe the number of charged particles coming out. And we denote the charged particle multiplicity by n_c.

The charged particle multiplicity n_c increases slowly with energy, the enregy dependence of n_c in p-p collision is shown in Fig. 2.6.1 . A parametrization at ISR energy (Thomé et al., 1977) is

$$n_c = 1.20 + 0.59 \ln E + 0.12 (\ln E)^2$$

where E is in Gev. Typical values of n_c at various energies are shown in Table 2.6.1 .

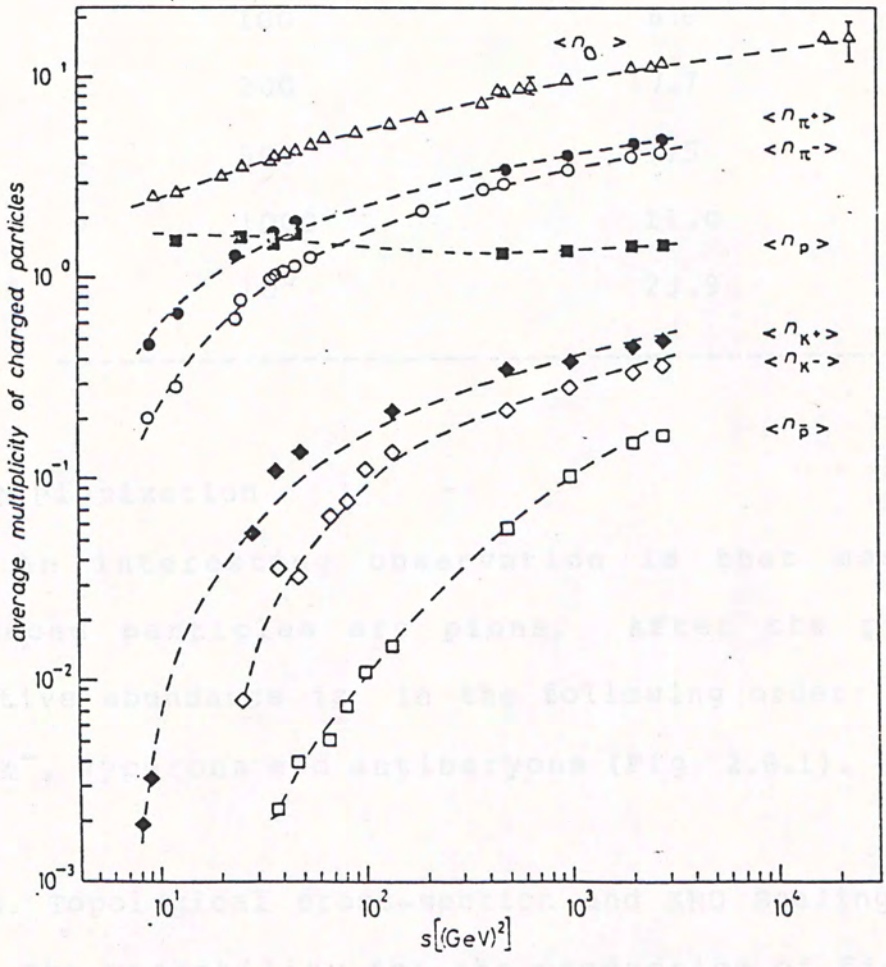

Fig. 2.6.1 The average multiplicity in p-p collisions for various types of charged particles vs s. Taken from Antinucci (1973).

Table 2.6.1 Energy Dependence Of Charged Multiplicity

Energy (GeV)	n_0
100	6.6
200	7.7
500	9.5
1000	11.0
10^5	23.9

2.6.2 Pionization

An interesting observation is that most of the produced particles are pions. After the pions, the relative abundance is in the following order: nucleons, K^+, K^-, hyperons and antibaryons (Fig. 2.6.1).

2.6.3. Topological cross-section and KNO Scaling

The probability for the production of final states with n charged prongs is called the topological cross-section σ_n . Fig. 2.6.2 shows the energy dependence of for p-p and $\pi^{\pm}p$ interactions (Whitemore, 1974). As the energy increases, σ_n for large n rises comparatively quickly and flattens out. That is, as energy grows, the inelastic cross-section is mainly made up of σ_n of large n.

In 1972, Koba Nielsen and Olesen (Koba et al., 1972)

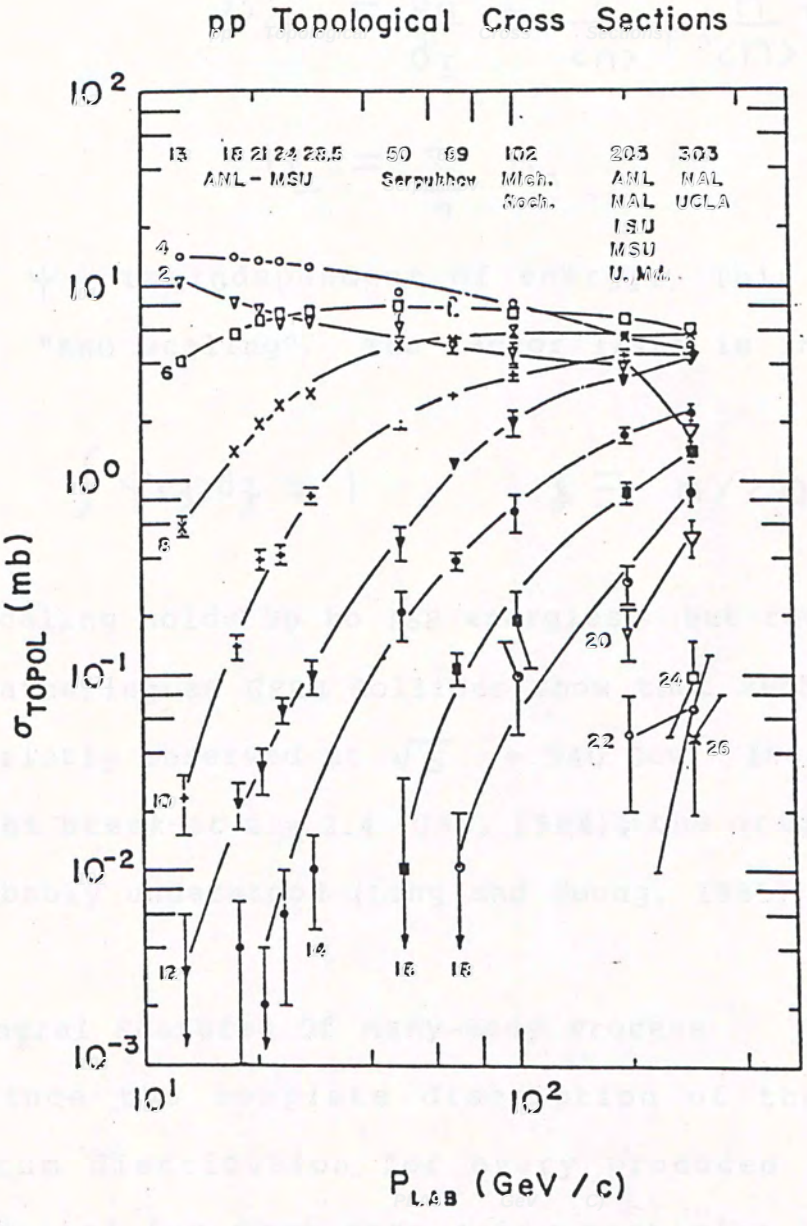

Fig. 2.6.2 Topological cross-section in p-p collision.
Taken from Whitemore (1974).

proposed that in the high energy limit $\langle n \rangle \sigma_n / \sigma_I$ is only a function of $n/\langle n \rangle$ i.e.

$$P(n) \equiv \frac{\sigma_n}{\sigma_I} = \frac{1}{\langle n \rangle} \psi\left(\frac{n}{\langle n \rangle}\right)$$

$$\sigma_I = \sum_n \sigma_n$$

where ψ is independent of energy. This is the so-called "KNO scaling". The factor $1/\langle n \rangle$ is inserted such that

$$\int \psi(z) dz = 1 , \qquad z \equiv n/\langle n \rangle$$

This scaling holds up to ISR energies. But recent data on $p\text{-}\overline{p}$ scattering at CERN Collider show that such scaling is not strictly observed at $\sqrt{s}$ = 540 Gev. Indeed there is a slight break at z = 2.4 (UA5, 1984), the origin of which is probably understood (Ling and Young, 1985).

2.7 General Features Of Many-Body Process

Since the complete discription of the angle and momentum distribution for every produced particle is impractical for more than a few particles in the final state, we have to find ways to summarize or condense these distribution.

2.7.1 Peyrou Plot

The Peyrou plot, though is rather old fashioned,

provides a simple and instructive way to study many-body final state reactions. It shows the momentum distribution of the particles for a single channel in the centre of mass. The ordinate is P_T, the momentum component of the secondary particle perpendicular to the direction of the incident particle. And the abscissa is P^*_1, the momentum component in the centre of mass along the direction of the incident particle. As an example Fig. 2.7.1 is the Peyrou plot (Czyzewski, 1968) for the produced nucleons, pions from $K^- p$ interactions at 10 Gev/c. These plots lead to the following observations:

(1) In general the particle momenta are not isotropic in the centre of mass frame. There is a sharp cut off in transverse momentum.

(2) The produced particles tend to have the same quantum number and momentum as the incident particle. It is called the leading particle effect. This is most evident for the proton in the figure.

2.7.2 One-Particle Inclusive Spectrum

The simplest approach to describe multiparticle production process is the one-particle inclusive spectrum. It concentrates on processes in which a given particle is produced but nothing is asked about the other particles which may also be present in this final state. For example the reaction:

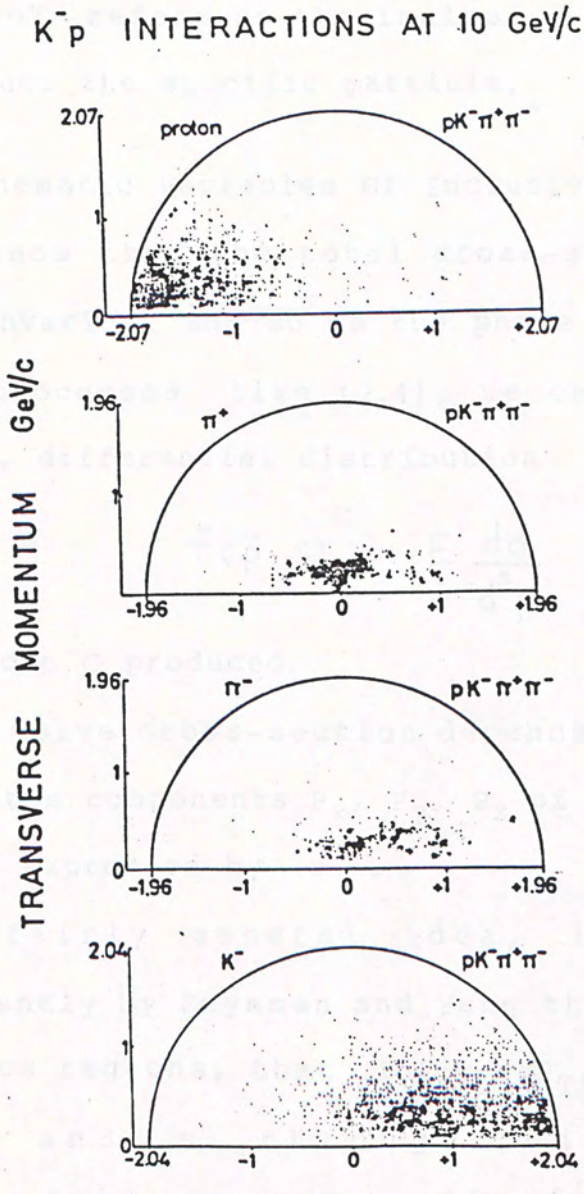

Fig. 2.7.1 Peyrou plot for K^-p interaction at 10 GeV/c. Taken from Czyzewski (1968).

$$A + B \quad \longrightarrow \quad C + X \qquad (2.4)$$

where X stands for whatever else is produced. The word "inclusive" refers to the inclusion of all final states that produce the specific particle.

2.7.3 Kinematic Variables Of Inclusive Reactions

We know that the total cross-section, σ_{tot} , is a Lorentz invariant and so is the phase space factor d^3p / E. For processes like (2.4), we can define a Lorentz invariant, differential distribution

$$f(\bar{p}, s) = E \frac{d\sigma}{d^3p}$$

for particle C produced.

This inclusive cross-section depends on four variables, the momentum components P_x, P_y, P_z of C and the incident energy as expressed by s .

On fairly general idea, it was predicted independently by Feynman and Yang that at least in some kinematics regions, that f (P_l, P_T, s) should depend on P_l and s through the combination

$$x = 2P_l / \sqrt{s}$$

at large s. This scaling concept is described fully in the following sections.

Rapidity is another extremely useful variable. It is defined as

$$y = \frac{1}{2} \ln \left(\frac{E + P_l}{E - P_l} \right)$$

The advantages of y are as follows :

(1) to move from one reference frame (y) to another (y') by means of a Lorentz transformation, one finds $y' = y + Y$ where $Y = \ln \gamma(1+\beta)$, and γ , β are the usual Lorentz parameters. So the shape of the distribution in y does not change but only shifts by Y.

(2) The relation between x and y is

$$x = \frac{\sqrt{m^2 + p_T^2}}{E} \sinh y$$

for the region near x = 0, the use of y spreads this region out and is therefore more convenient for data presentation. To illustrate this, we reproduce in Fig. 2.7.2 a comparison between the different variables, shown are plots in y and c.m. momentum P_l. Comparing Fig. (a) and (b) we see that most of the rapidity range is mapped into small x region.

The rapidity variable y requires a momentum measurement. It is much easier to measure the angle, so experimentalists often use the pseudo-rapidity η ,

$$\eta = -\ln(\tan \frac{\theta}{2})$$

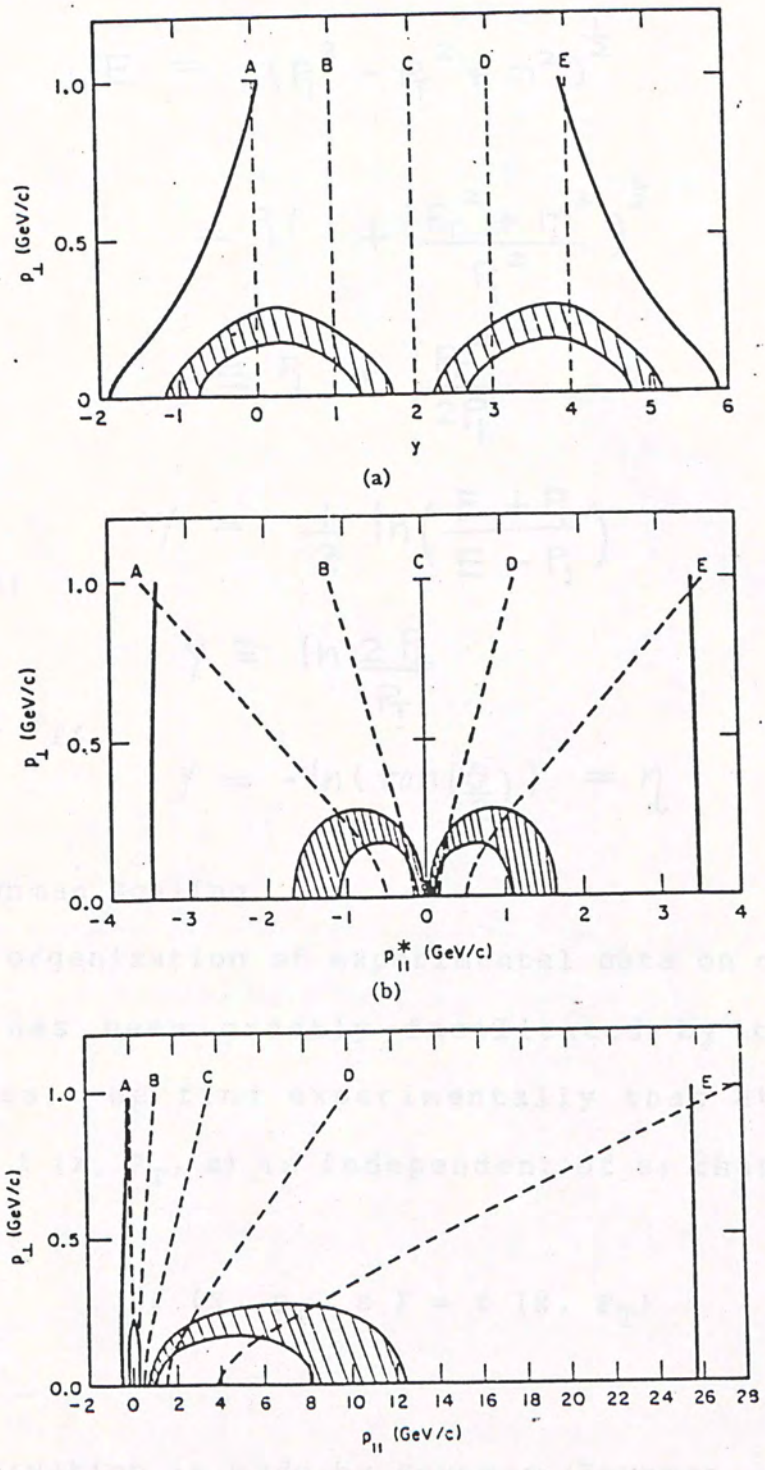

Fig. 2.7.2 Comparison of rapidity with c.m. and lab momenta plots at P_{lab} = 25.6 GeV/c. Taken from Detar (1971).[1]

where θ is the emitting angle

Note that η becomes equal to y for $P_T >> m$.

$$E = (P_l^2 + P_T^2 + m^2)^{\frac{1}{2}}$$

$$= P_l\left(1 + \frac{P_T^2 + m^2}{P_l^2}\right)^{\frac{1}{2}}$$

$$\cong P_l + \frac{P_T^2}{2P_l} \qquad (2.5)$$

Since

$$y = \frac{1}{2}\ln\left(\frac{E + P_l}{E - P_l}\right)$$

With (2.5)

$$\Rightarrow \quad y \cong \ln\frac{2P_l}{P_T}$$

For small P_T,

$$y = -\ln\left(\tan\left(\frac{\theta}{2}\right)\right) = \eta$$

2.7.4 Feynman Scaling

The organization of experimental data on one-particle spectra has been graetly facilitated by the scaling hypotheses. We find experimentally that at very high energies f (x, P_T, s) is independent of s; that is

$$f\ (x,\ P_T,\ s\ ) = f\ (x,\ P_T)$$

This observation is made by Feynman (Feynman, 1969). Fig. 2.7.3a illustrates the scaling behavior in p-p scattering. This scaling holds up to ISR energies. Fig. 2.7.3b shows the deviation from scaling at large P_T .

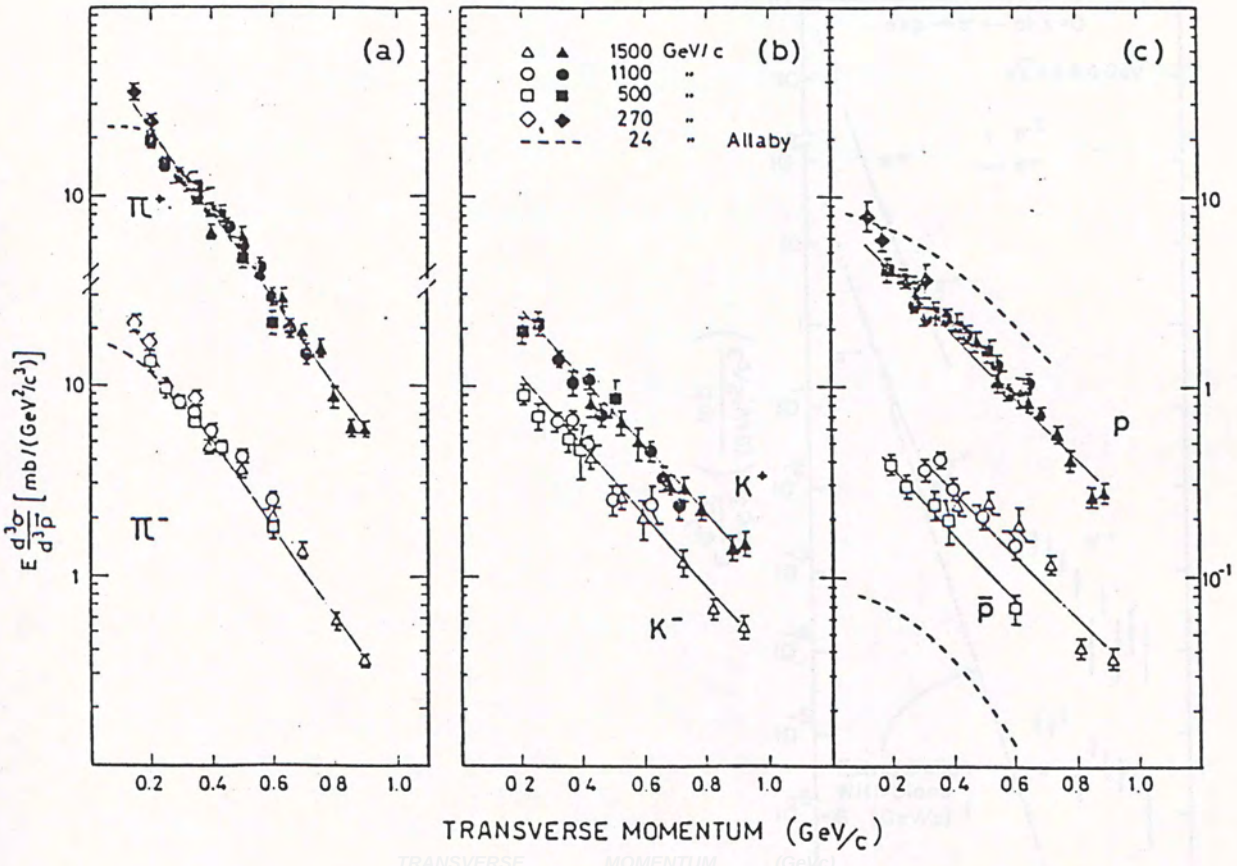

Fig. 2.7.3a Illustration of Feynman scaling. Taken from Bertin (1972).

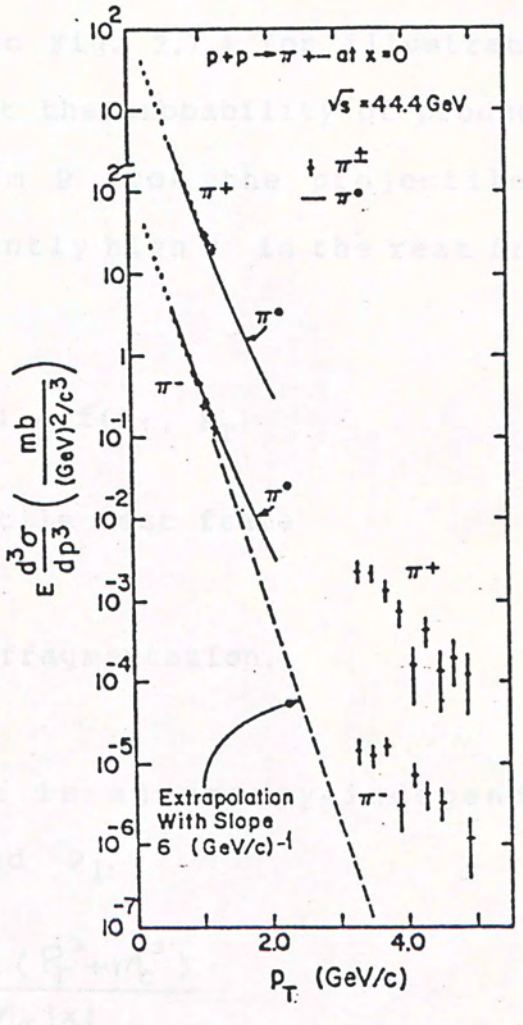

Fig. 2.7.3b Deviation from Feynman scaling.
Taken from Banner (1972).

2.7.5 Hypothesis Of Limiting Fragmentation

Benecke, Chou, Yang and Yen (1969) proposed that the emitted particles result from the fragmentation of the original particles. Refer to Fig. 2.7.4 for illustration. And they further assumed that the probability of producing a fragment C with momentum P from the projectile is independent of s at sufficiently high s in the rest frame of the projectile.

$$f(P_l, P_T, s) = f(P_l, P_T)$$

P_l is measured in the projectile rest frame

This is called the limiting fragmentation.

At high energies there is an energy-independent relationship between x and P_l.

$$P_l = \frac{m_a^2 x^2 - (P_T^2 + m_c^2)}{2 m_a |x|}$$

Therefore in the lab frame the function f (x, P_T, s) approaches an asymptotic limit for large s. It predicts Feynman scaling at the fragmentation region.

2.7.6 Experimental Test Of Limiting Fragmentation

The fragmentation picture can be carried a little further by proposing that the projectile and the target

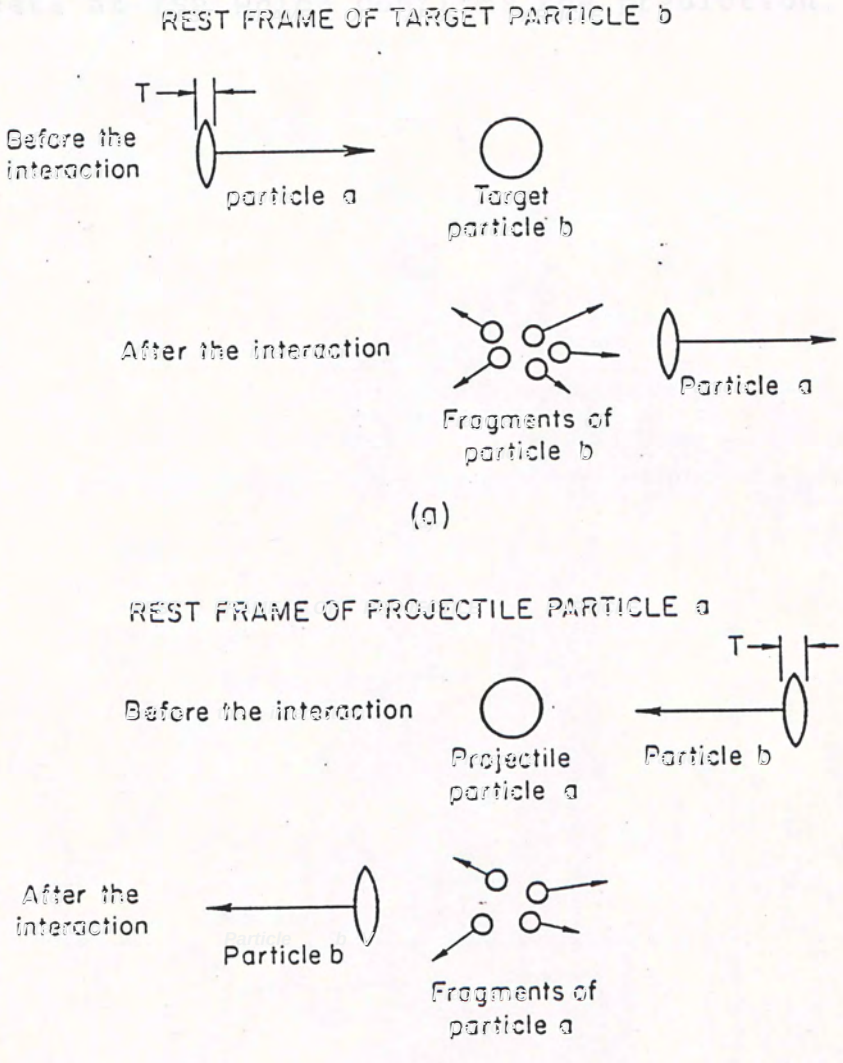

Fig. 2.7.4 Illustration of the fragmentation picture. Taken from Perl (1973).

fragment, each in its own reference system, independent of the other. One would then expect to find a plateau in the central region in rapidity plot, and the height will only depend on the overall normalization. Fig 2.7.5 shows experimental data at ISR which confirms the prediction.

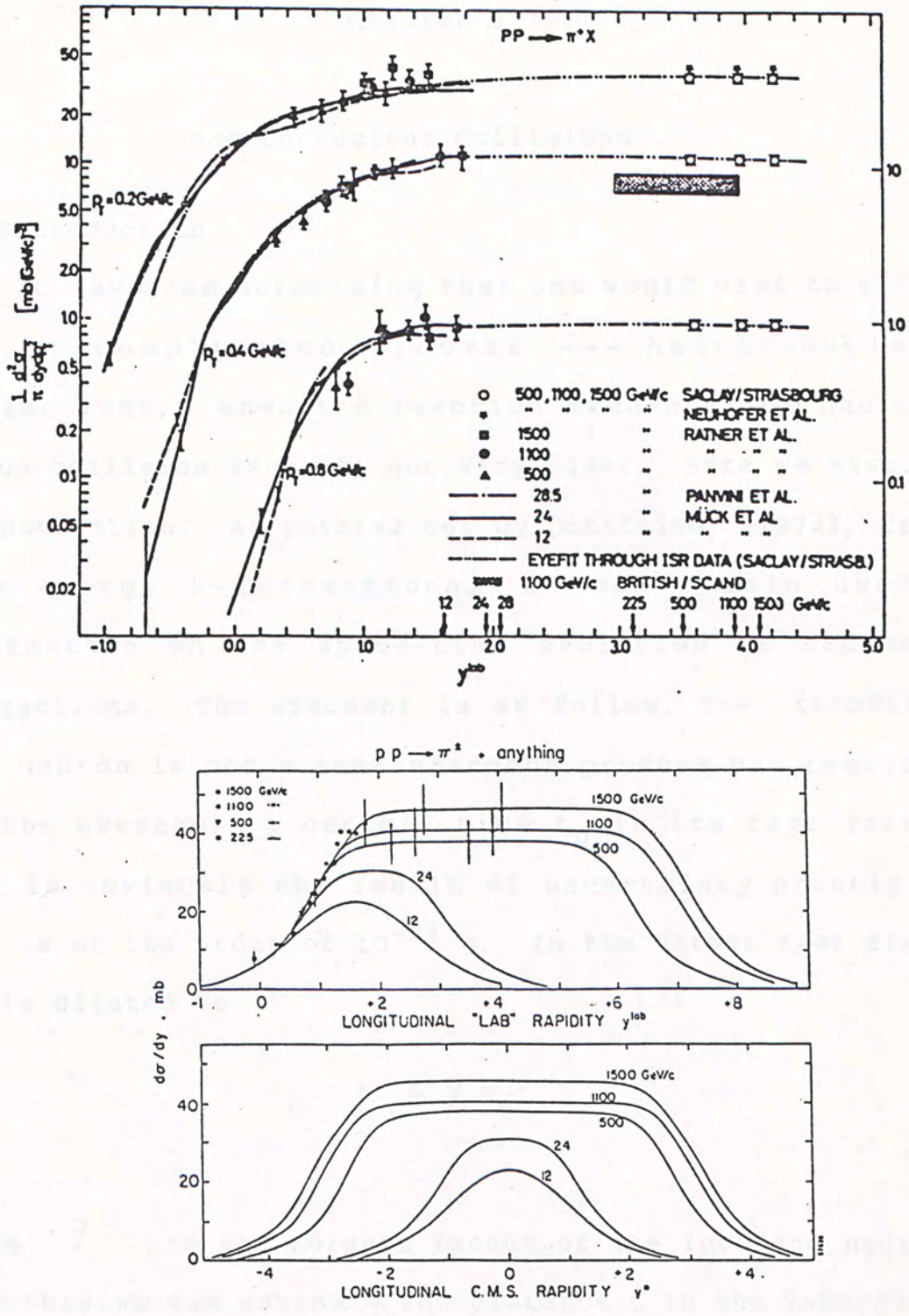

Fig. 2.7.5 Example of plateau in central region. Taken from Horn (1973).

Chapter 3

Hadron-Nucleus Collisions

3.1 Introduction

It may seem surprising that one would want to study such a complicated process --- hadron-nucleus interactions, when the reaction mechanism of hadron-hadron collision is still not very clear. Here we discuss the motivation. As pointed out by Gottfried (1974), from high energy h-A reactions, we can obtain useful information on the space-time evolution of hadronic interactions. The argument is as follow. The formation of a hadron is not a instantaneous process but requires (on the average) a certain time t_o in its rest frame, this is obviously the result of uncertainty principle. t_o is of the order of 10^{-24} s. In the target rest frame t_o is dilated to

$$t' = \gamma t_o$$

where γ is the Lorentz factor of the incident hadron. From this we can estimate the distance L in the laboratory frame over which particles are produced.

$$\gamma \sim \frac{\sqrt{s}}{2M}$$

$$L \sim \frac{\sqrt{s}}{2}$$

where M is a nucleon mass, s is in GeV and L in fm. For a high-energy hadron the Lorentz factor and the corresponding formation distance L might be very large and exceeds the nucleus size. For example at $\sqrt{s}$ = 100 Gev, L is of the order of 100 fm. Thus the important conclusion follows: the produced particles are formed outside of the nucleus. And the intra-nuclear process is sensitive to the short-time behaviour of hadronic interactions, and yields information that cannot be inferred directly from the corresponding h-h process where only the asymptotic final states are observed.

3.2 Hadron-Nucleus Cross-Sections

3.2.1 Total Cross-Section

The energy dependence of σ_{tot} is weak. For incident energy ranges from 30 - 300 Gev, it hardly changes. Fig. 3.2.1 shows the A dependence of σ_{tot} in this enengy range for various incident hadrons.

The A dependence is a measure of showdowing in h-A interaction. In the absence of shadowing, σ_{tot} should be proportional to the total number of nucleons --- A. On the other hand, in case of maximum shadowing, σ_{tot} should be proportional to the area of the nucleus, hence to $A^{2/3}$.

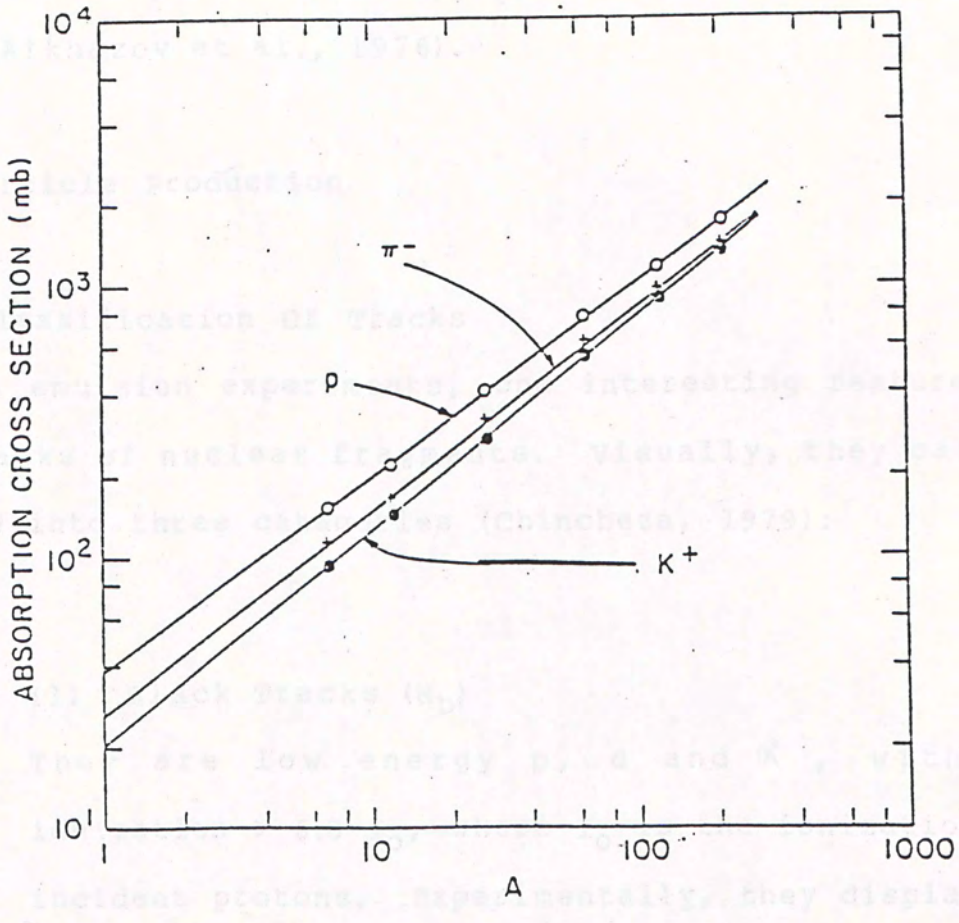

Fig. 3.2.1 The A dependence of h-A total cross-section. Taken from Carroll (1979).

3.2.2 Elastic Scattering

The elastic differential cross-section of h-A scattering has a very similar structure as h-h collisions. It is dominated by diffraction peaks. Fig. 3.2.2 shows the experimantal angular distributions for proton elastic scattering on ^{40}Ca , ^{42}Ca , ^{44}Ca and ^{48}Ti (Alkhazov et al., 1976).

3.3 Particle Production

3.3.1 Classification Of Tracks

In emulsion experiments, one interesting feature is the tracks of nuclear fragments. Visually, they can be divided into three catagories (Chincheza, 1979):

(1) Black Tracks (N_b)

They are low energy p, d and α , with an ionization > 6.8 I_o, where I_o is the ionization of incident protons. Experimentally, they display an almost isotropic angular distribution.

(2) Grey Tracks (N_g)

They are mainly protons in the energy range 40 - 400 Mev, and have an ionization between 1.4 and 6.8 I_o. They usually peak forward. And they are believed to originate from the recoiling nucleons in the nucleus.

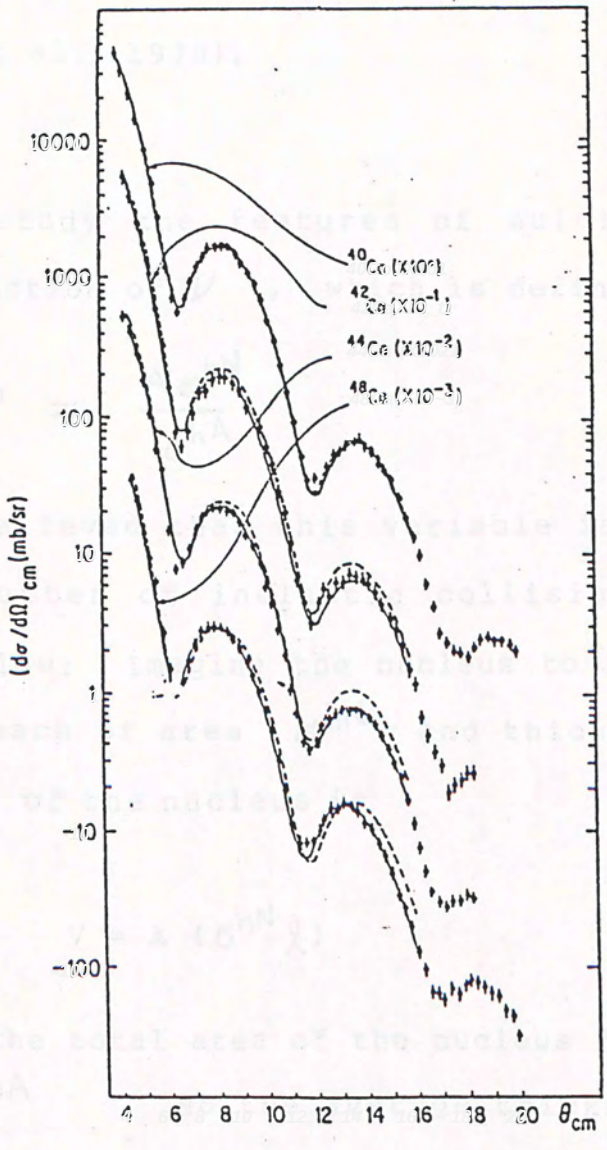

Fig. 3.2.2 Elastic differential cross-section for p-A scattering. Taken from Alkhazov (1976).

(3) Shower Particles (N_s)

They are mainly pions with $\beta = v/c > 0.7$

Fig. 3.3.1 shows the correlation between these tracks at 400 Gev (Boos et al., 1978).

3.3.2 The Variable ν

We wish to study the features of multiparticle production as a function of ν, which is defined as

$$\nu = \frac{A\sigma^{hN}}{\sigma^{hA}} \qquad (3.1)$$

It is commonly believed that this variable is closely related to the number of inelastic collisions. The argument is as follow: Imagine the nucleus to be formed of A nucleons, each of area σ^{hN} and thickness ℓ. Then the volume V of the nucleus is

$$V = A(\sigma^{hN}\ell)$$

On the other hand the total area of the nucleus facing the beam is $\mathcal{A} = \sigma^{hA}$. So the average thickness $\langle t \rangle$ may be identified as

$$\langle t \rangle = V/\mathcal{A} = \frac{A\sigma^{hN}\ell}{\sigma^{hA}}$$

The average number of nucleons penetrated is then

$$\nu = \frac{\langle t \rangle}{\ell} = \frac{A\sigma^{hN}}{\sigma^{hA}}$$

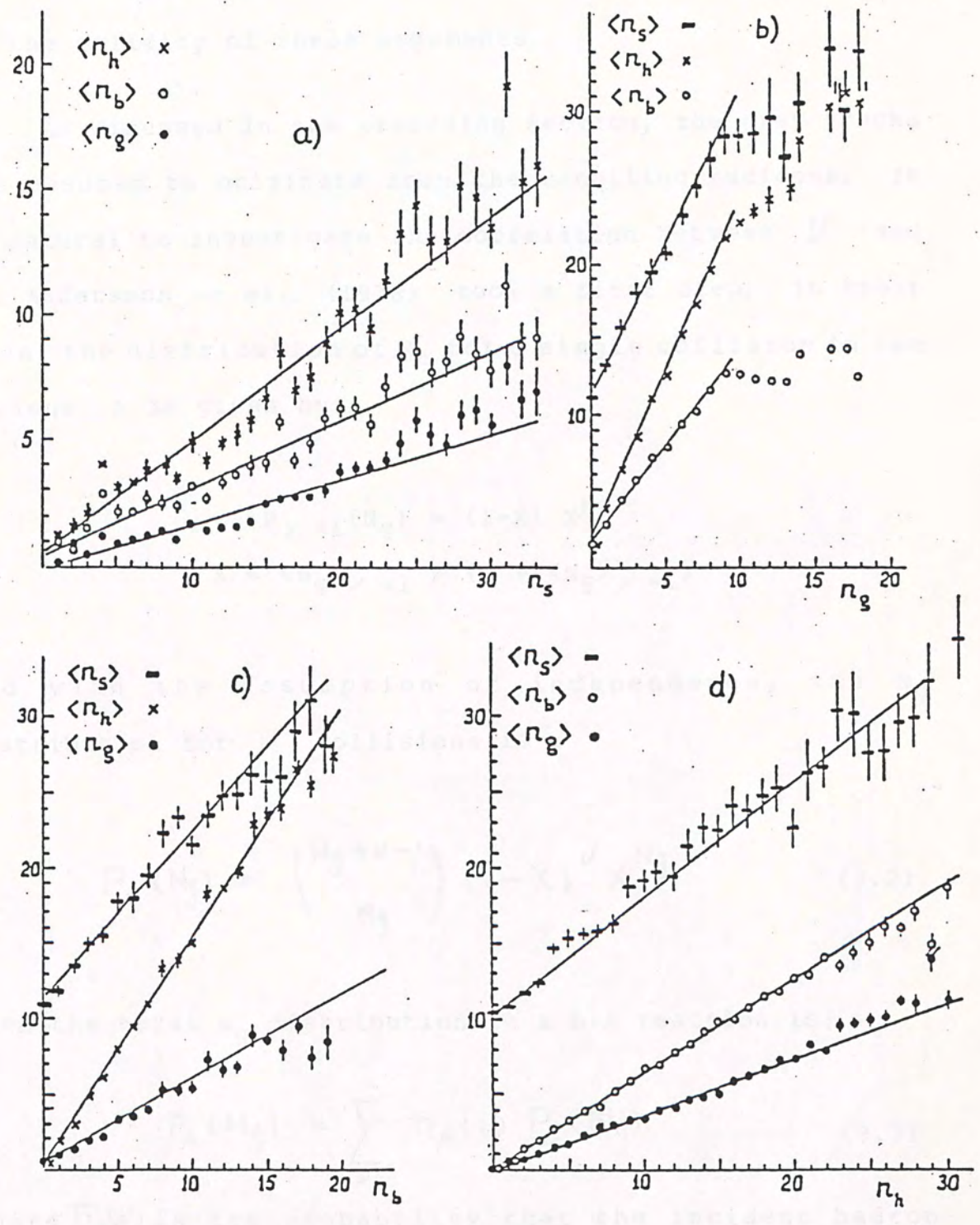

Fig. 3.3.1 Multiplicity correlations in p-A interactions at 400 GeV. Taken from Boos (1978).

This crude argument merely motivates the definition of ν . Analysis based on ν of course does not depend on the validity of these arguments.

As dicussed in the preceding section, the grey tracks are assumed to originate from the recoiling nucleons. It is natural to investigate the correlation between ν and N_g. Andersson et al. (1978) took a first step. In their model the distribution of N_g for a single collision in the nucleus A is given by:

$$P_{\nu=1}(N_g) = (1-X)\, X^{Ng}$$

$$X = \langle N_g \rangle_{\nu=1} / (1 + \langle N_g \rangle_{\nu=1})$$

And with the assumption of independence, the N_g distribution for ν collisions is :

$$P_\nu(N_g) = \binom{N_g+\nu-1}{N_g} (1-X)^\nu X^{N_g} \qquad (3.2)$$

Then the total N_g distribution in a h-A reaction is:

$$P_A(N_g) = \sum_\nu \pi_A(\nu)\, P_\nu(N_g) \qquad (3.3)$$

where $\pi_A(\nu)$ is the probability that the incident hadron collides ν times in the nucleus. It was taken from a Monte Carlo calculation with a Woods-Saxon nuclear density distribution.

The dotted curve in Fig. 3.3.3 predicted from Eq.

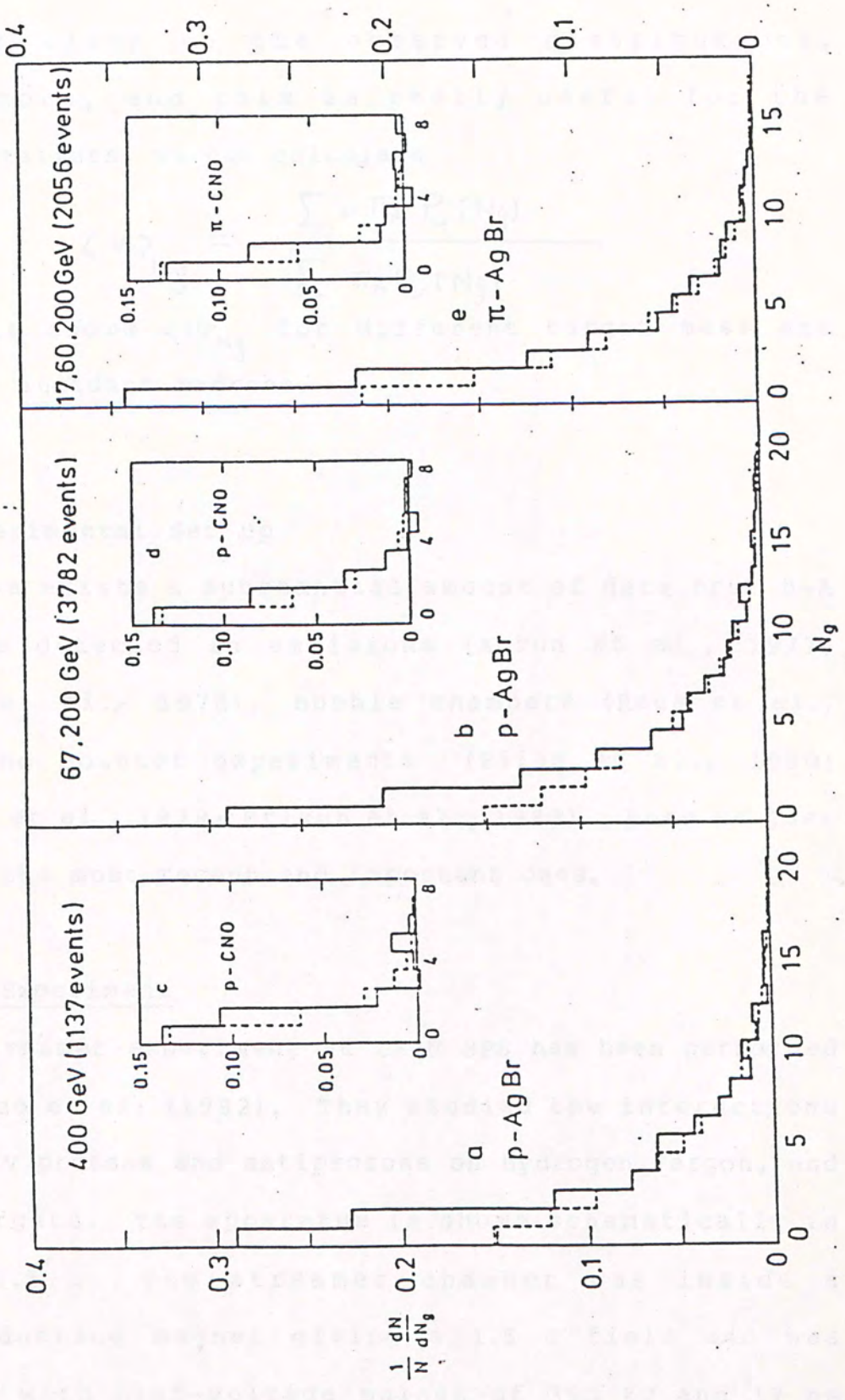

Fig. 3.3.3 Grey track distribution from p-Em reactions at 200 and 400 GeV compared with prediction from Andersson's model.

(3.3) is close to the observed distributions. Furthermore, and this is really useful for the experimentalists, we can calculate

$$\langle \nu \rangle_{Ng} = \frac{\sum \nu \pi_A P_\nu(N_g)}{\sum \pi_A P_\nu(N_g)}$$

Fig. 3.3.4 shows $\langle \nu \rangle_{Ng}$ for different target mass and different incident hadrons.

3.3.3 Experimental Set up

There exists a substantial amount of data from h-A reactions detected in emulsions (Anzon et al., 1977; Babecki et al., 1978), bubble chambers (Rees et al., 1983), and counter experiments (Elias et al., 1980; Faessler et al., 1979; Frisch et al., 1983). Here we just describe the most recent and important ones.

Streamer Experiment

A streamer experiment at CERN SPS has been performed by DeMarzo et al. (1982). They studied the interactions of 200 GeV protons and antiprotons on hydrogen, argon, and xenon targets. The apparatus is shown schematically in Fig. 3.3.5 . The streamer chamber was inside a superconducting magnet giving a 1.5 T field and was operated with high-voltage pulses of 350 kV and 12 ns duration. The nuclear target consisted of a tube filled with xenon or argon gas at 9 atm. . Fig. 3.3.6 shows a photograph of a proton-xenon interaction.

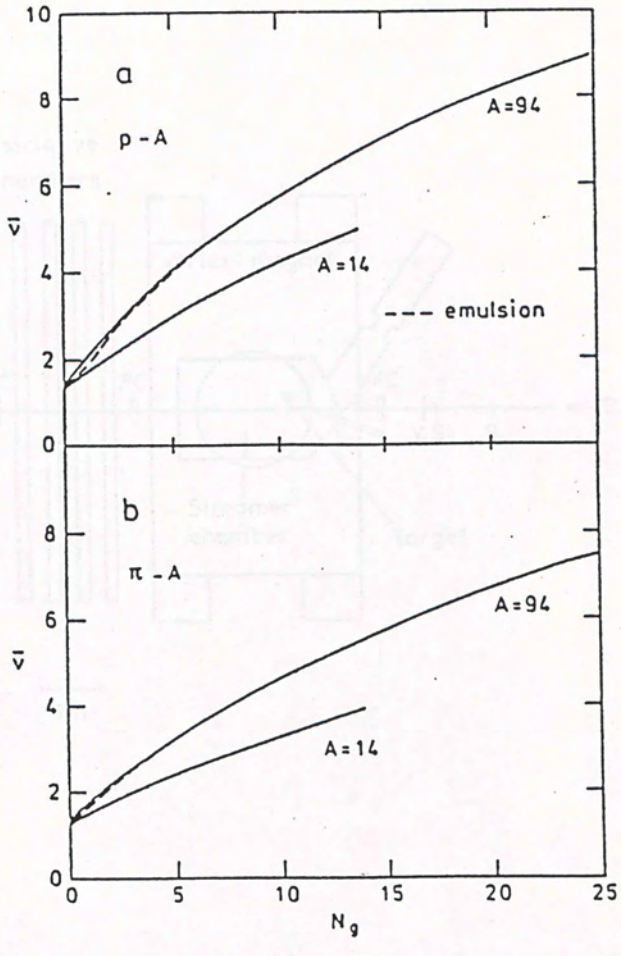

Fig. 3.3.4 $\bar{\nu}$ as a function of N_g for different nuclei. Taken from Andersson (1978).

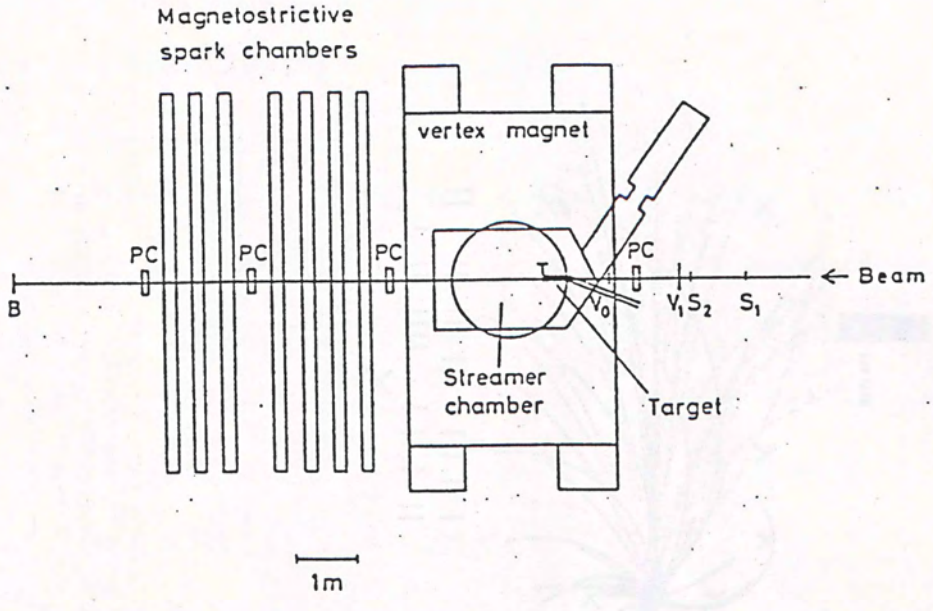

Fig. 3.3.5 Layout of DeMarzo's streamer experiment. Taken from DeMarzo (1982).

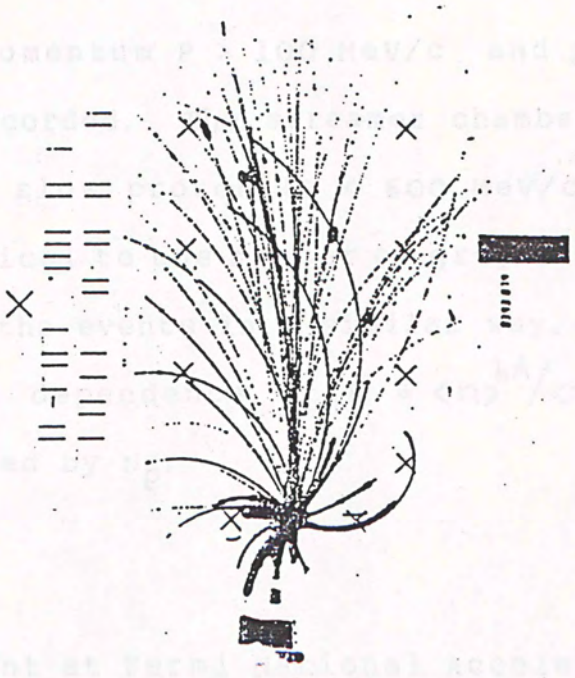

Fig. 3.3.6 Photograph of a p-Xe interaction at 200 GeV. Taken from DeMarzo (1982).

The setting error in space was 0.4 mm. And the measuring accuracy in momentum is $\Delta P / P = 0.0025 P$ (P in GeV/c). Range, ionization, and decay signature were used to identify particles. From the ionization information pions could be distinguished from protons.

Since both the energy and momentum of the produced particle can be measured, true rapidity distribution can be given. (Fig. 3.3.7).

All protons with momentum P > 100 MeV/c and pions with P > 35 MeV/c are recorded. The streamer chamber can identify the number of slow proton (P < 600 MeV/c) N_p. This number is not identical to the number of grey tracks; however it characterize the events in a similar way. Fig. 3.3.8 presents the ν dependence of $R = \langle n \rangle^{hA} / \langle n \rangle^{hN}$, where ν is characterized by N_p.

Counter Experiment

A counter experiment at Fermi National Accelerator Laboratory has been performed by Barton et al. (1983). Various hadrons (protons, pions, kaons) at 100 GeV are used to bombard nuclear targets (C, Al, Cu, Ag, Pb). The inclusive production of different particles was measured over a momentum range of $30 < P < 88$ GeV/c and transver-momentum range $0.18 < P_T < 0.5$ GeV/c.

The incident beam could transport up to $6 * 10^6$ hadron / pulse into the experimental area. The beam consisted of pions, kaons, and protons with the ratio

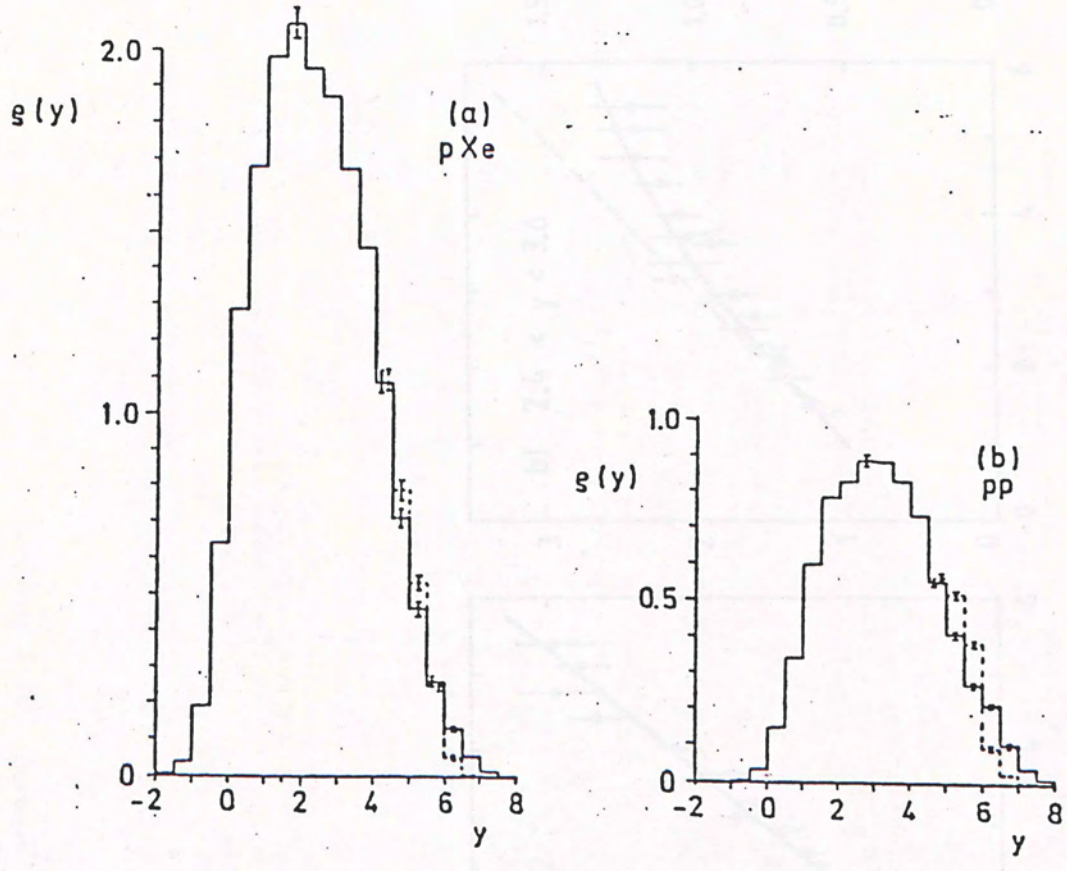

Fig. 3.3.7 Rapidity distribution for (a) p-Xe, (b) p-p interaction at 200 GeV. Taken from DeMarzo (1982).

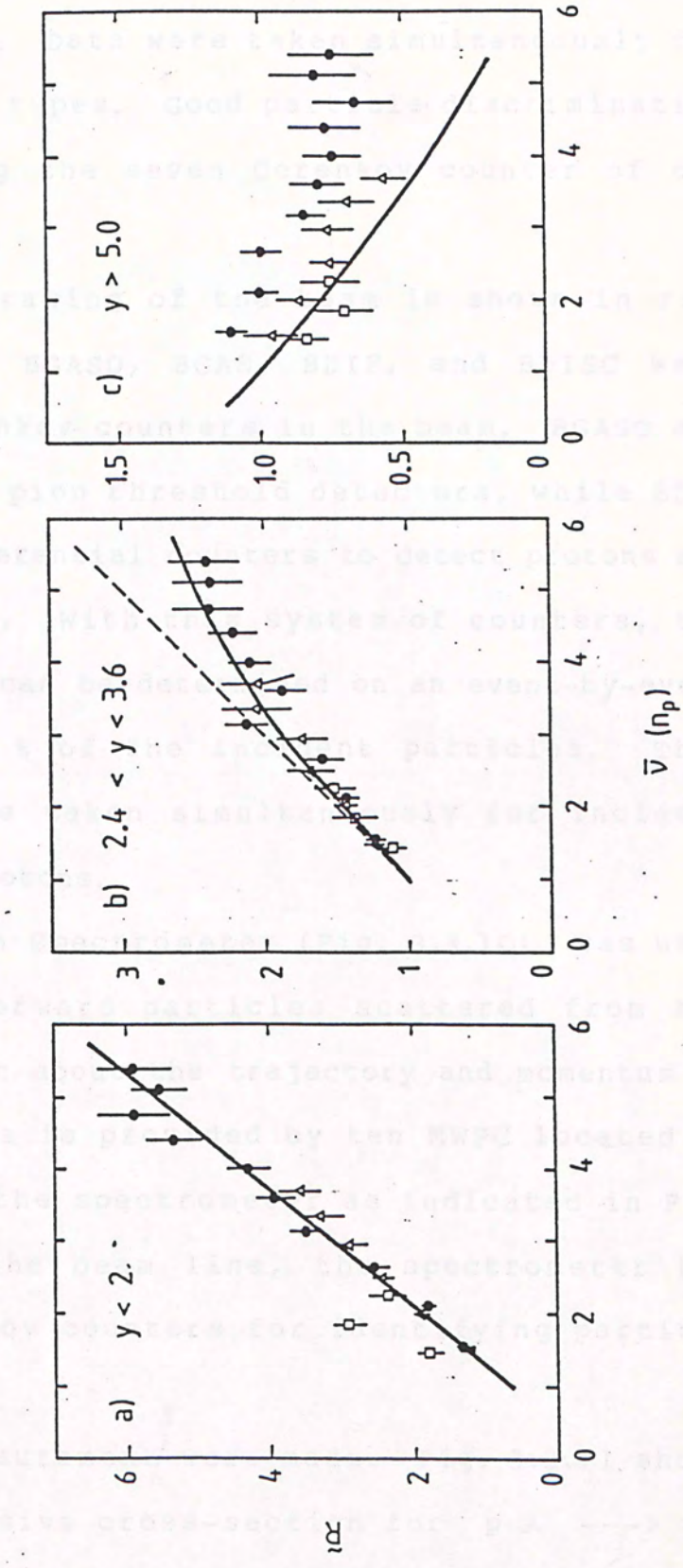

Fig. 3.3.8 R vs $\bar{\nu}$ in different rapidity region.
Taken from DeMarzo (1984b).

0.60 : 0.04 : 0.36 . Data were taken simultaneously for different reaction types. Good particle discrimination was achieved using the seven Cerenkov counter of the facility.

A schematic drawing of the beam is shown in Fig. 3.3.9 . Elements BGASO, BGAS, BDIF, and BDISC were pressured gas Cerenkov counters in the beam. BGASO and BGAS were the beam pion threshold detectors, while BDIF and BDISC were differential counters to detect protons and kaons respectively. With this system of counters, the beam particle type can be determined on an event-by-event basis for over 95 % of the incident particles. This allowed data to be taken simultaneously for incident pions. kaons and protons.

The Single Arm Spectrometer (Fig. 3.3.10) was used to analyze fast forward particles scattered from the target. Information about the trajectory and momentum of scattered particles is provided by ten MWPC located at four places along the spectrometer as indicated in Fig. 3.3.10 . As in the beam line, the spectrometer had several gas Cerenkov counters for identifying particle type.

Extensive measurements were made. Fig. 3.3.11 shows the measured inclusive cross-section for p A ---> p X plotted as a function of x.

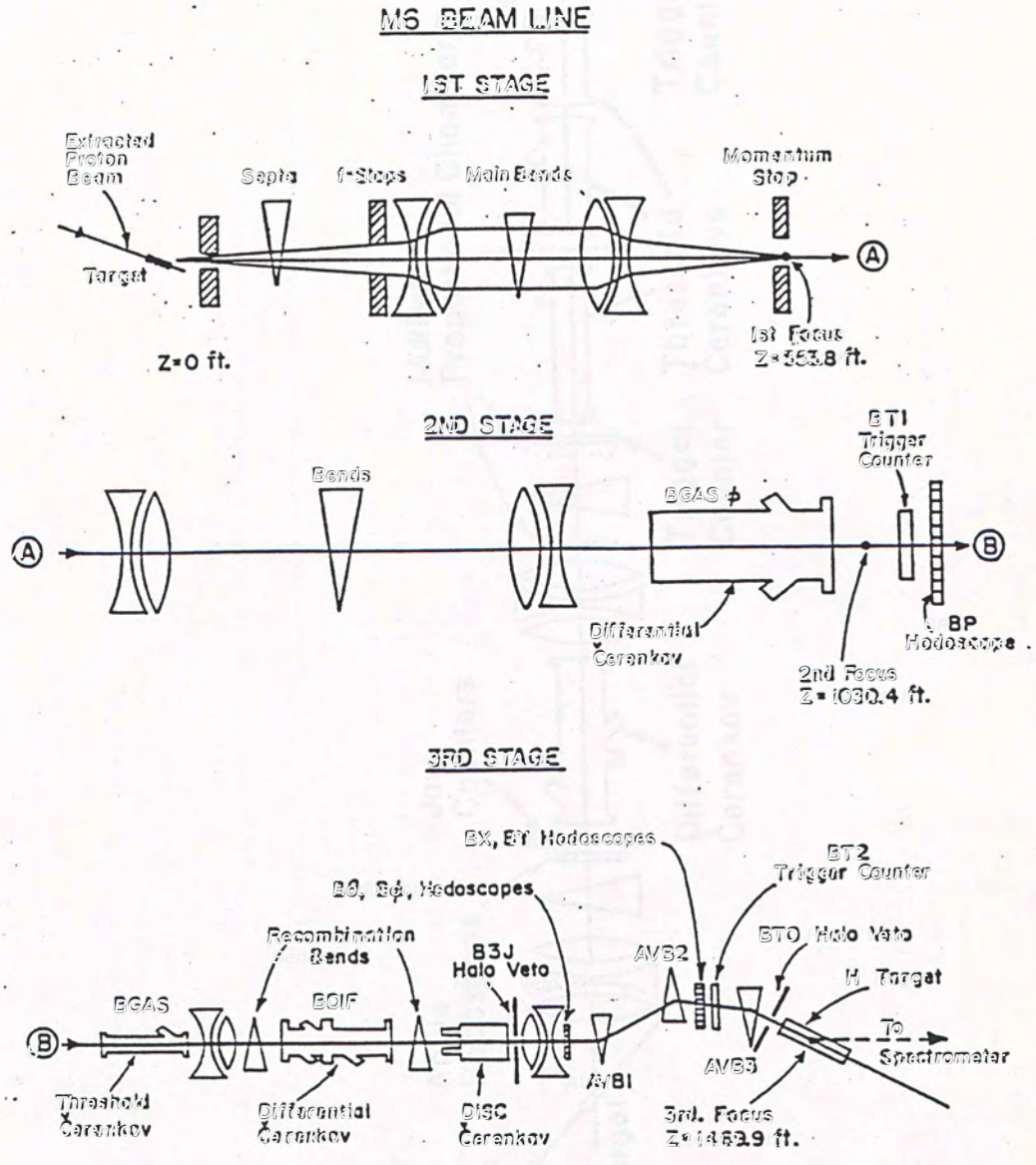

Fig. 3.3.9 Layout of Barton's counter experiment. Taken from Ayres (1977).

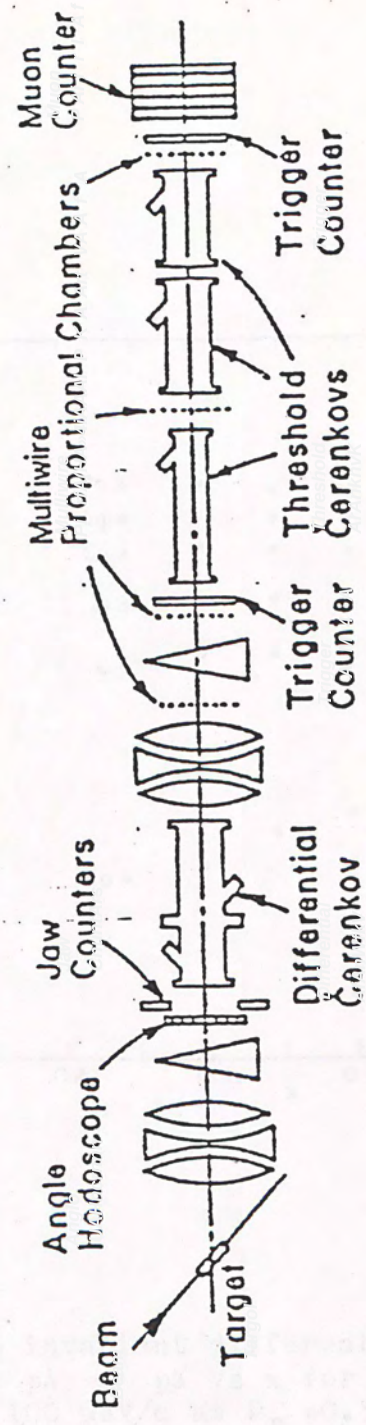

Fig. 3.3.10 Diagram of the Single Arm Spectrometer. Taken from Ayres (1977).

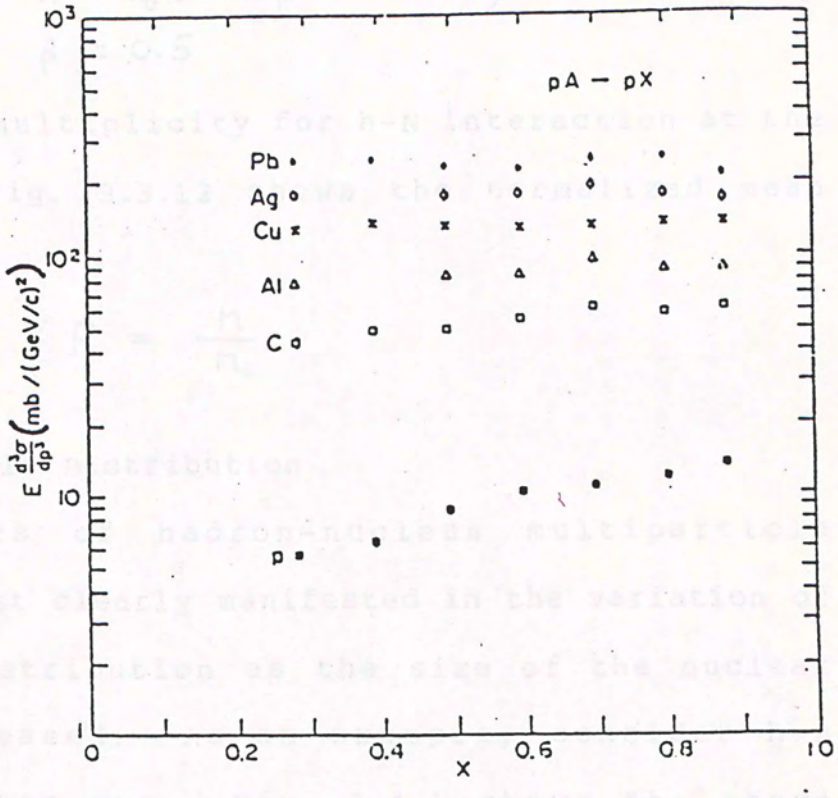

Fig. 3.3.11 The invariant differential cross-section for pA $\rightarrow$ pX vs x for an incident momentum of 100 GeV/c at P_T =0.3 GeV/c. Taken from Barton (1983).

3.3.4 Multiplicity

On nuclei, the mean multiplicity n of the secondary particles are higher than on free nucleons. It is experimentally well established that n increases with ν as

$$n = n_0(1 + \beta(\nu - 1)), \qquad (3.4)$$
$$\beta \simeq 0.5$$

where n_0 is the multiplicity for h-N interaction at the same energy. Fig. 3.3.12 shows the normalized mean multiplicity

$$R = \frac{n}{n_0}$$

3.4 Single Particle Distribution

The physics of hadron-nucleus multiparticle production is most clearly manifested in the variation of the rapidity distribution as the size of the nuclear target is increased. As an example, consider h-A collisions at 200 Gev. Fig. 3.4.1 shows the above variation.

Qualitatively the data suggest that the produced particles concentrate more at the target fragmenatation region ($y < 2$) as the size of the target increases. And there seems to be no multiplication at the projectile fragmentation region. To manifest this point we plot the quantity

$$R(\eta) \equiv (dn/d\eta)_{hA} \Big/ (dn/d\eta)_{hN}$$

in different N_g groups at 400 Gev in Fig. 3.4.2 . It can

something missing

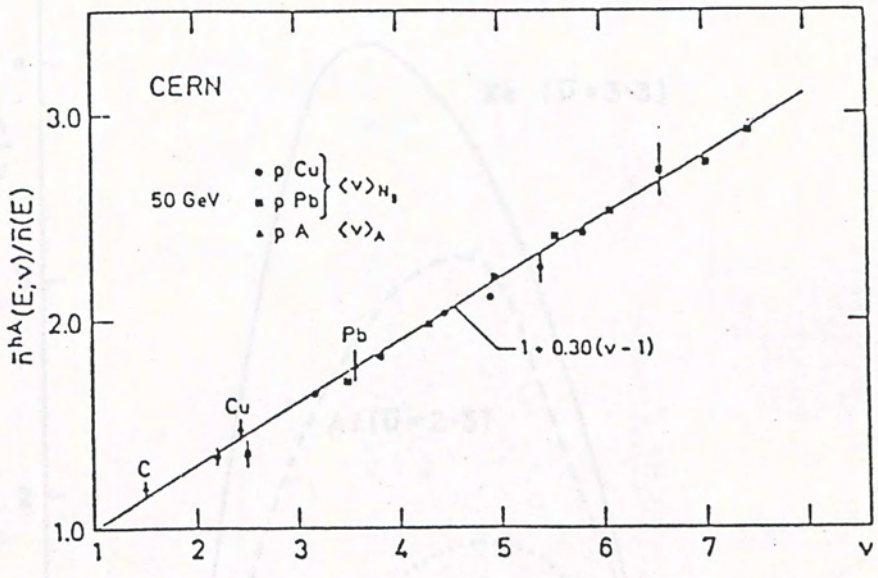

Fig. 3.3.12 The normalized mean multiplicity as a function of ν . Taken Chao (1983).

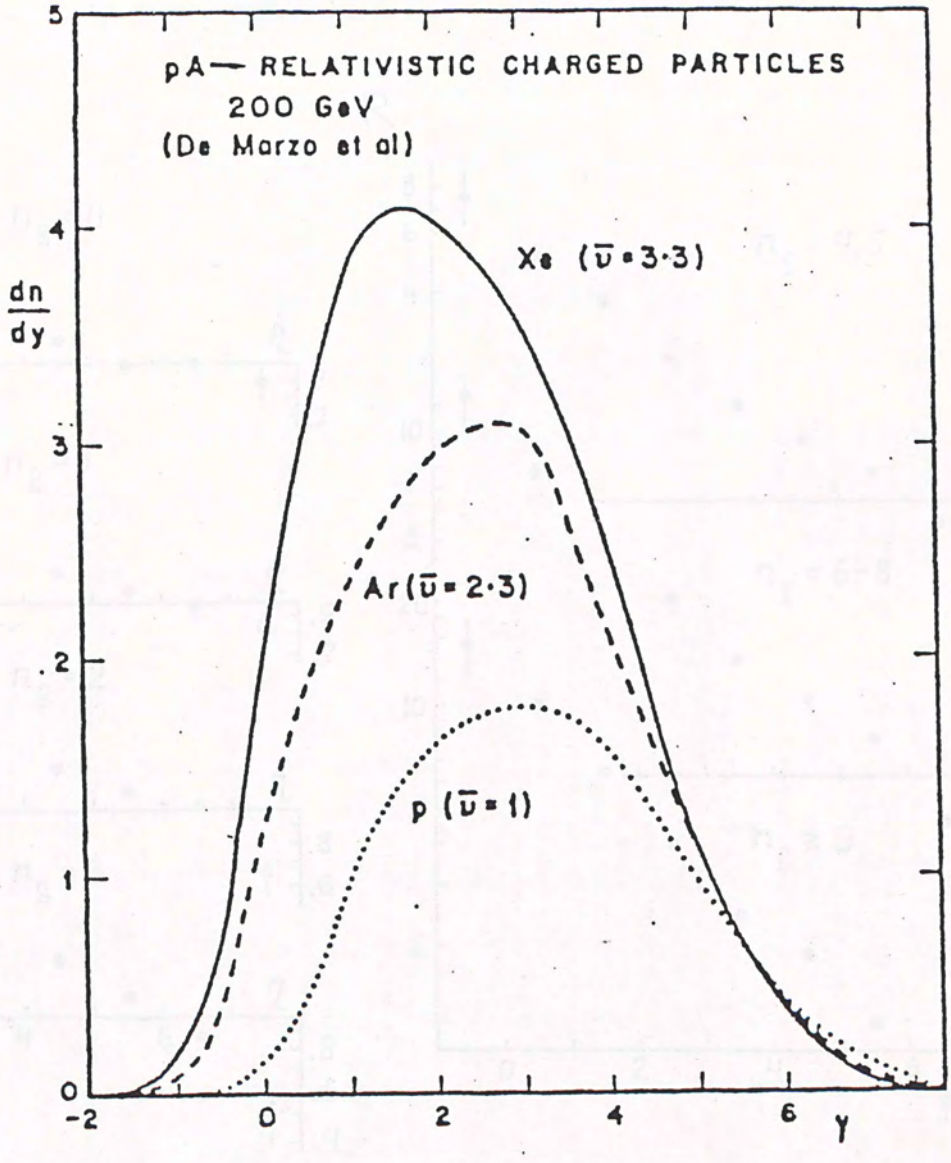

Fig. 3.4.1 Rapidity distribution in 200 GeV p-A reactions. Taken from Busza (1984).

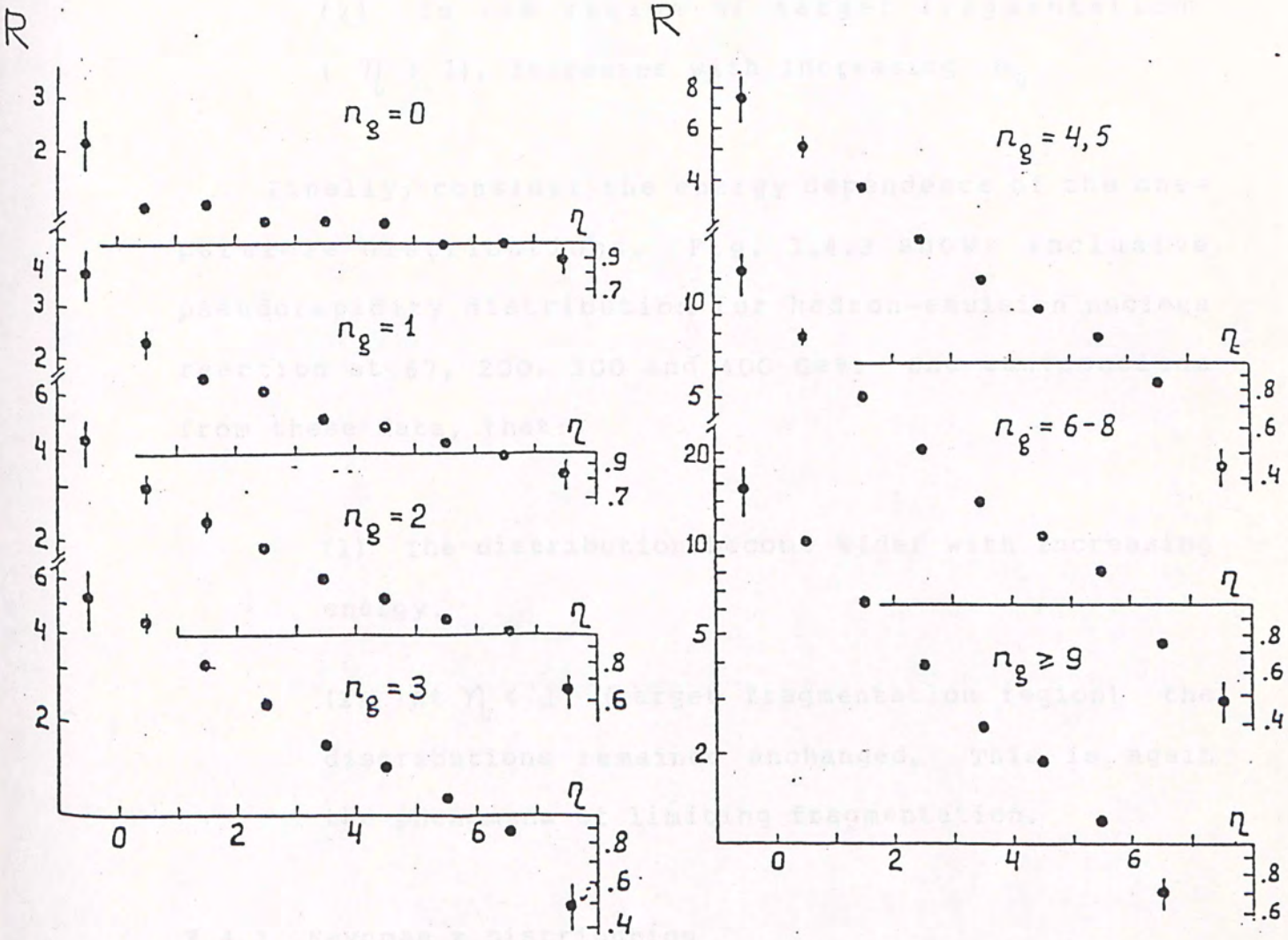

Fig. 3.4.2 The ratio R as a function of η at 400 GeV. Taken from Boos (1978).

(1) In the projectile fragmentation region ($\eta < 1$), decreases with increasing N_g.

(2) In the region of target fragmentation ($\eta > 1$), increases with increasing N_g

Finally, consider the energy dependence of the one-particle distributions. Fig. 3.4.3 shows inclusive pseudorapidity distributions for hadron-emulsion nucleus reaction at 67, 200, 300 and 400 Gev. One can conclude from these data, that:

(1) The distribution become wider with increasing energy.

(2) At $\eta < 1$ (target fragmentation region) the distributions remained unchanged. This is again the phenomena of limiting fragmentation.

3.4.1 Feynman x Distribution

Several experiments, designed to investigate the projectile fragmentation mechanism, have studied the invariant differential cross-section $E d\sigma/d^3p$ for h-A collisions as a function of x. Fig. 3.3.11 is the result from Barton et al. (1983) . It should be noted that the peak near x = 1 is flattened as A increases. This means that the leading particle effect is obvious for p-p

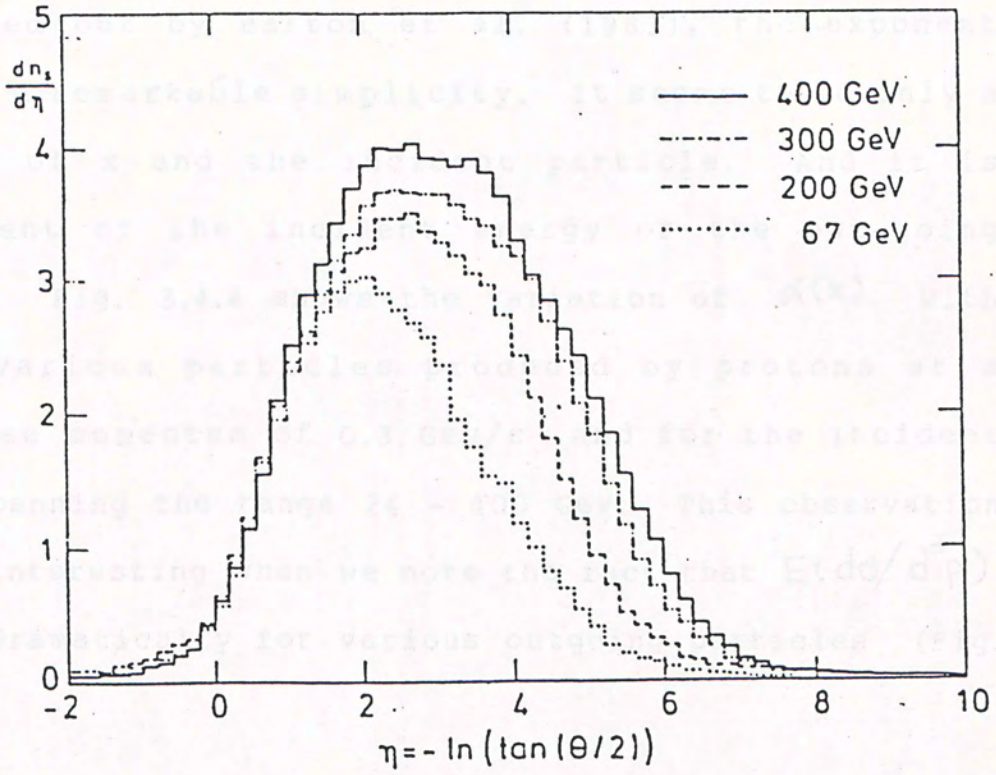

Fig. 3.4.3 The inclusive shower-particle pseudo-rapidity distribution in the target nucleus frame. Taken from Otterlund (1978).

that the leading particle effect is obvious for p-p interaction but is reduced for larger A.

To investigate the A dependence of $E(d\sigma/d^3p)$, it is a common practice to parametrize it as

$$E\frac{d\sigma}{d^3p} = \sigma_c(x)A^{\alpha(x)}$$

As pointed out by Barton et al. (1983), the exponent exhibits a remarkable simplicity. It seems to be only a function of x and the incident particle. And it is independent of the incident energy or the out-going particle. Fig. 3.4.4 shows the variation of $\alpha(x)$ with x for various particles produced by protons at a transverse momentum of 0.3 Gev/c and for the incident energy spanning the range 24 - 400 Gev. This observation is very interesting when we note the fact that $E(d\sigma/d^3p)$ differs dramatically for various outgoing particles (Fig. 3.4.5) .

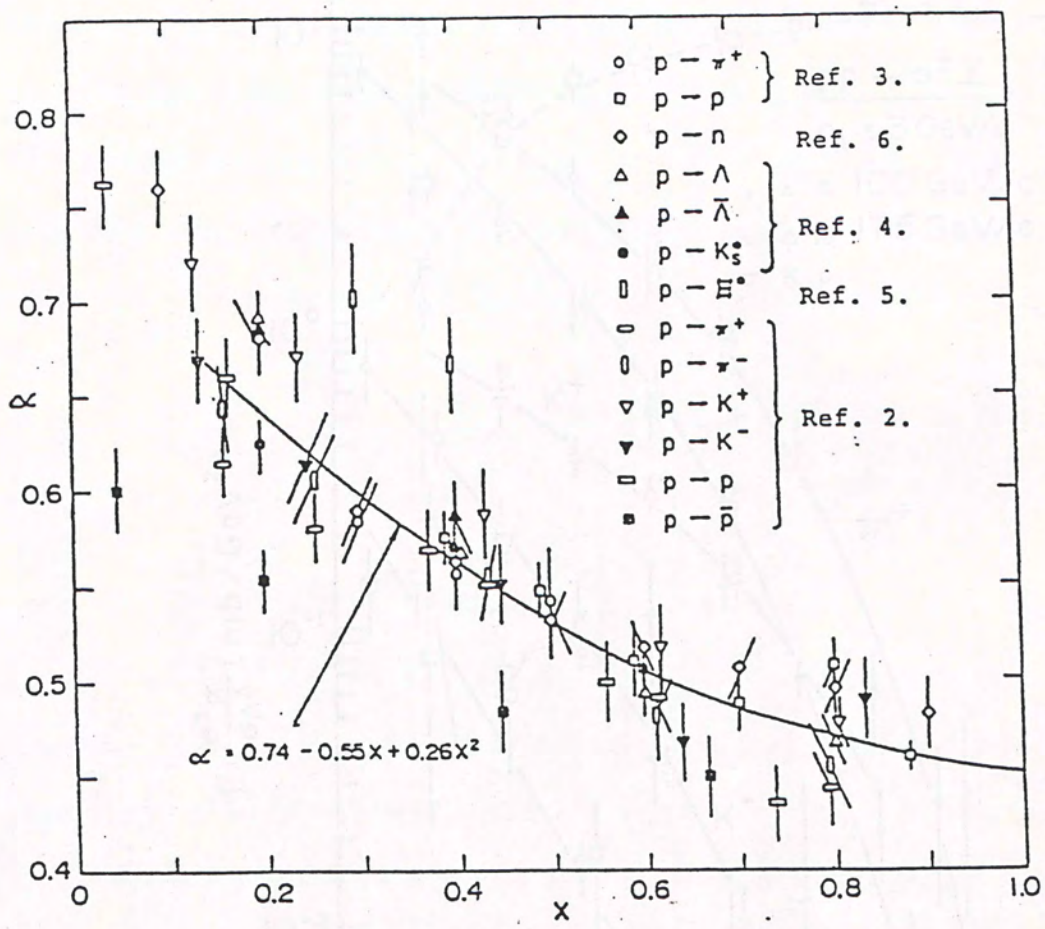

Fig. 3.4.4 The parameter α as a function of x for various proton-induced reactions at P_T = 0.3 GeV/c. Taken from Barton (1983).

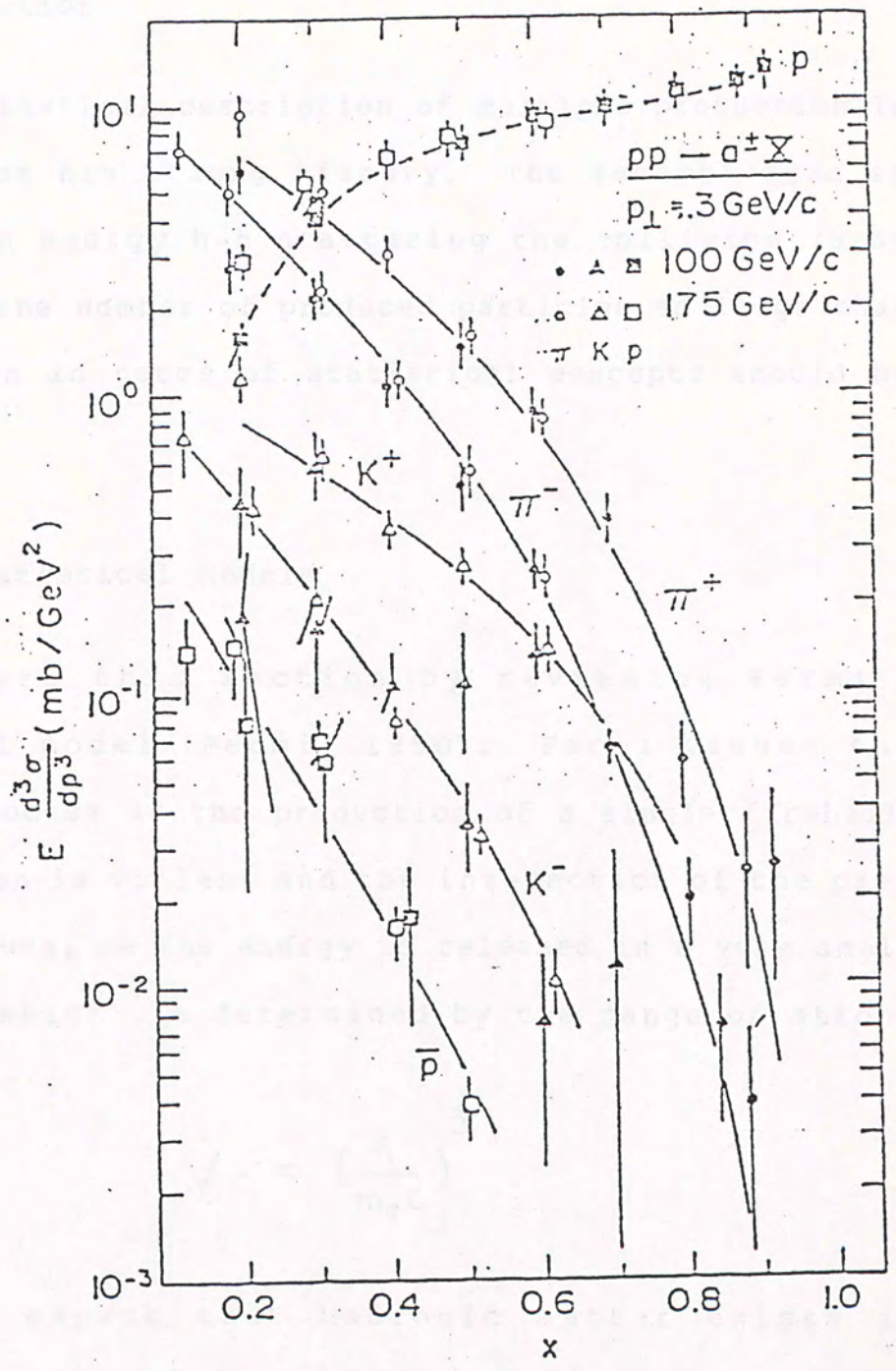

Fig. 3.4.5 The invariant cross-sections for $pp \longrightarrow hX$ at P_T = 0.3 GeV/c. Taken from Busza (1983).

Chapter 4

Partition Temperature Model

4.1 Introduction

The statistical description of multiple production in h-h collision has a long history. The general idea is that in high energy h-h scattering the collision is so violent and the number of produced particles so large that a description in terms of statistical concepts should be possible.

4.2 Early Statistical Models

We start this section by reviewing Fermi's statistical model (Fermi, 1950). Fermi viewed the collision process as the production of a single fireball. The collision is violent and the interaction of the pion field is strong, so the energy is released in a very small volume V, which is determined by the range of strong interaction :

$$V = \left(\frac{\hbar}{m_\pi c}\right)^3$$

So we may expect that hadronic matter exists in thermodynamic equilibrium and then decays into observable particles.

The basic hypothesis is that the observed real

particles appear with a distribution corresponding to black-body radiation. At a temperature T, the most probable number of photons per unit frequency per unit volume in a black-body is

$$\frac{dN}{d\nu} = \left(\frac{8\pi\nu^2}{c^3}\right)\left(e^{h\nu/kT} - 1\right)^{-1} \qquad (4.1)$$

The pions are taken to be highly relativistic and the pions number density per unit energy is

$$\frac{dN}{dE} = \text{const.} * E^2 \left(e^{E/kT} - 1\right)^{-1} \qquad (4.2)$$

where E is the energy of the pion.

The average multiplicity <N> is given by integrating Eq. (4.2)

$$\langle N \rangle = \text{const.} * \int_0^\infty \frac{E^2}{e^{E/kT} - 1}\, dE$$

$$\simeq \text{const.} * (kT)^3 \qquad (4.3)$$

Similarly, the energy density U is given by

$$U = \text{const.} * \int_0^\infty \frac{E^3}{e^{E/kT} - 1}\, dE$$

$$\simeq \text{const.} * (kT)^4 \qquad (4.4)$$

U is also given by

$$U = \sqrt{s} / V$$

After some arithmetic, the average multiplicity is

$$\langle N \rangle = \text{const.} * s^{3/8} \qquad (4.5)$$

which is in crude agreement with experiment.

Fermi's basic idea regarding the use of statistical mechanics in h-h collision is fruitful. But some of his assumptions and quantitative predictions are inconsistent with experiment. Eq. (4.2) will give an isotropic angular distribution, which obviously contradicts experiment.

Also, as pointed out by Pomeranchuk (1951), at the moment of collision, we can speak of the number of particles only in a limited sense, since the interaction range of the particle is greater than the overall dimension of the system.

On the basis of this idea, Landau (1953) developed the hydrodynamical model. Since in the early stage of the production process, the 'mean free path' is very small compared to the dimension of the system, the process of expansion must have a hydrodynamic character. His work can be summarized as:

(1) Since the incident hadron is highly relativistic, the volume V in which the energy is released is Lorentz contracted in the direction

of the hadron's motion. In the first stage, a contracted disk is formed. The disk has a initial temperature T_o and energy density U_o determined by Eq. (4.4)

(2) This disk constitutes the initial stage of the hydrodynamical expansion; the quantities U and T decrease during the expansion process.

(3) When the temperature reaches a certain final value m_π (pion rest mass), the decay of the system into real particles sets in.

An important prediction of the model is the angular distribution of the secondary particles $dn/d\eta$ in the centre mass frame

$$\frac{dn}{d\eta} = \frac{N\exp(-\eta^2/2L)}{\sqrt{2\pi L}} \qquad (4.6)$$

where

$$L = 0.56 \ln E_o + 1.6 \ln(2/(N+1)) + 1.6 \qquad (4.7)$$

and E_o is in GeV .

Fig. 4.2.1 shows the predictions for $dn/d\eta$ from Eq. (4.6) for different incident energy E_o.

4.3 Partition Temperature

Recently Chou, Yang and Yen (1985) suggested that

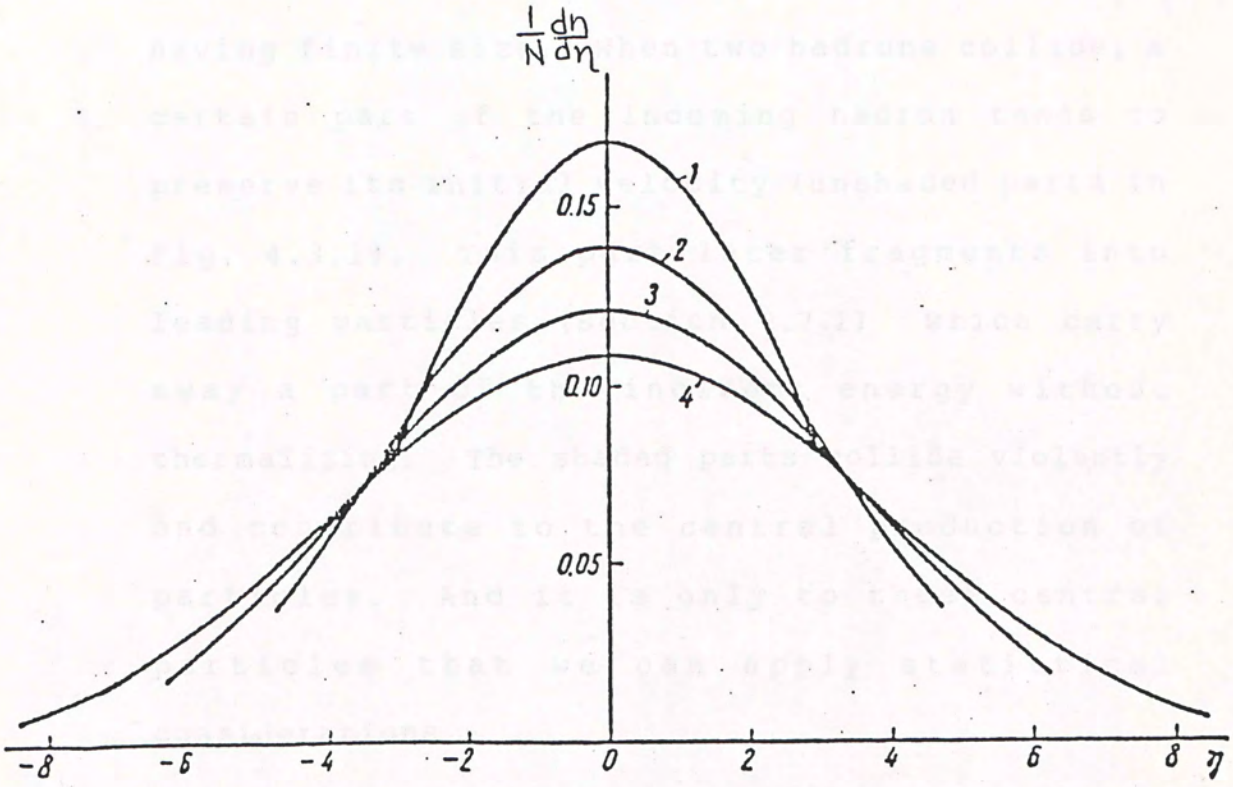

Fig. 4.2.1 Calculated normalized pseudo-rapidity distribution for various incident energy: 1. 1TeV, 2. 100 TeV, 3. 10 TeV, 4. 10 TeV. Taken from Milekhin (1959).

the statistical idea on h-h collision should be modified by the following well-known empirical observations:

(1) Leading particles

In their opinion, hadrons are geometrical object having finite size. When two hadrons collide, a certain part of the incoming hadron tends to preserve its initial velocity (unshaded parts in Fig. 4.3.1). This part later fragments into leading particles (Section 2.7.1) which carry away a part of the incident energy without thermalizing. The shaded parts collide violently and contribute to the central production of particles. And it is only to these central particles that we can apply statistical considerations.

(2) Cut-off on transverse momentum

As disscused in Section 2.7.1 , it is a well supported observation that the transverse momentum distribution can be described by exp $(-\alpha p_T)$.

Their model is as follow. Let the number of produced particle be n_o, and hE_o be the energy available for particle production. Now our system has n_o particles and energy hE_o, and such an isolated system can be described by a microcanonical ensemble.

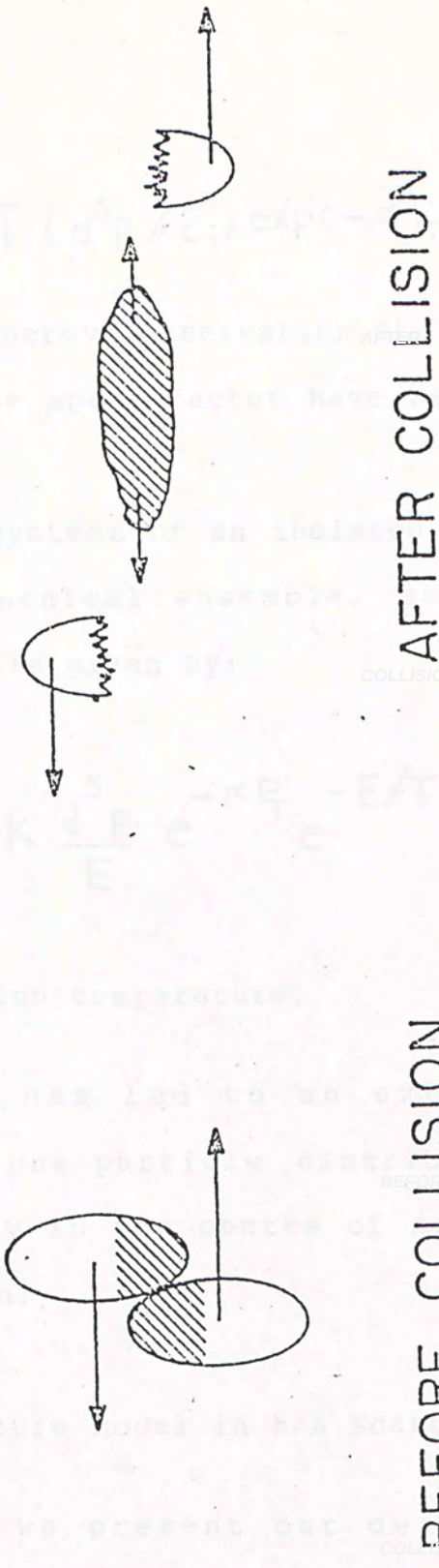

Fig. 4.3.1 Schematic diagram depicting multiparticle production process. Taken from Chou (1985).

$$\delta(\sum E_i - E_0 h) \prod_i (d^3 P_i / E_i) \exp(-\alpha P_{Ti})$$

where in addition to energy conservation the cut-off on P_T and the invariant phase space factor have been explicitly inserted.

As usual the subsystems of an isolated system can be described with a canonical ensemble, so the single-particle distribution is given by:

$$dn = K \frac{d^3 P}{E} e^{-\alpha P_T} e^{-E/T} \qquad (4.8)$$

where T is the partition temperature.

This approach has led to an extremely good description of the one-particle distribution in p-p scattering at 540 GeV in the centre of mass. See Fig. 4.3.2 for illustration.

4.4 Partition Temperature Model in h-A Scattering

In this section we present our own work on the partition temperature model in h-A scattering (Li and Young, 1986) which attempts to generalize the very good results obtained by Chou, Yang and Yen's work in h-h scattering.

4.4.1 Formalism and Result

At high energies, the de Broglie wavelength of the projectile is much smaller than the nuclear radii and the

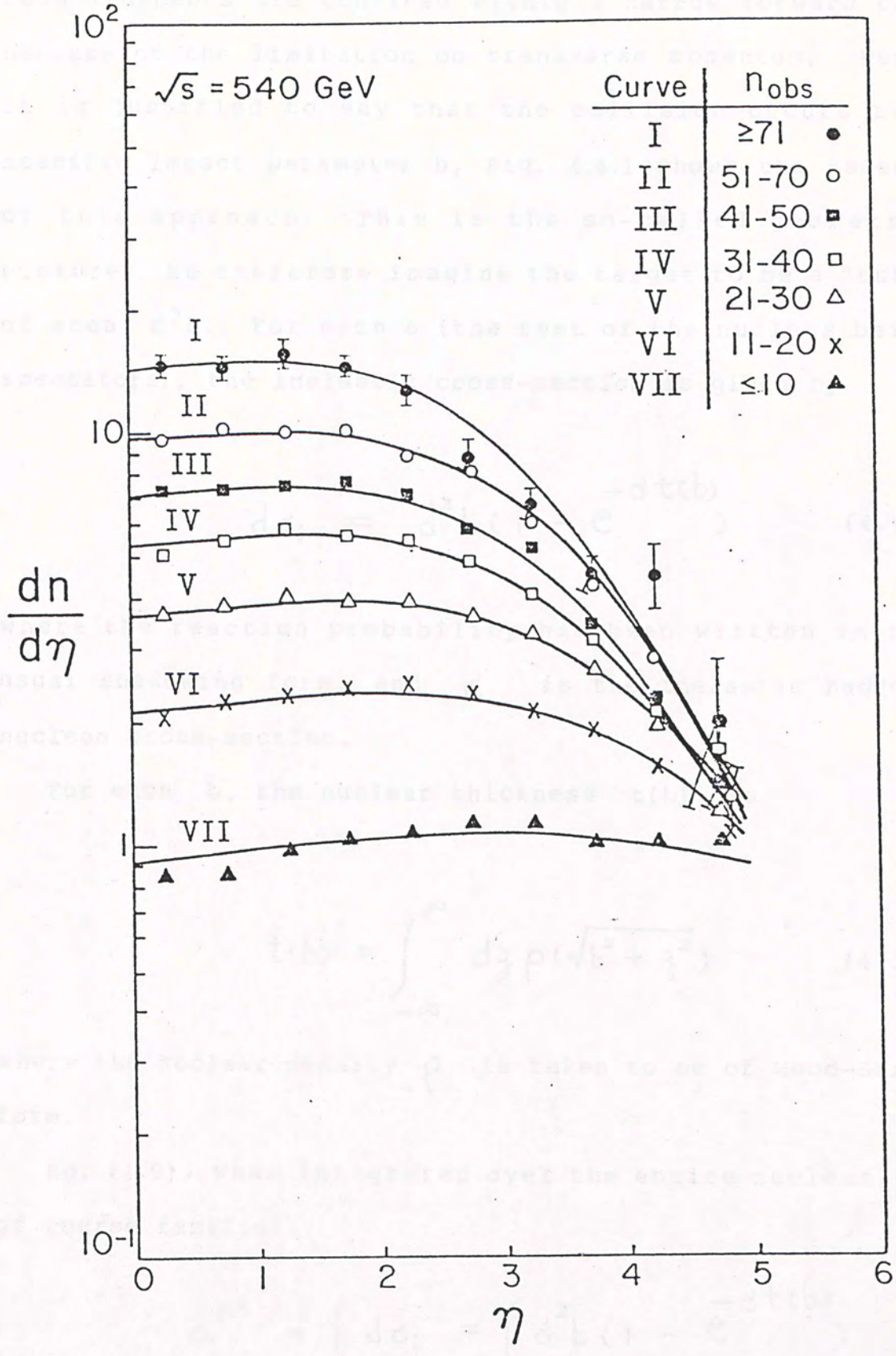

Fig. 4.3.2 Predicted pseudo-rapidity distribution form Eq. (4.8). Taken from Chou (1985).

beam fragments are confined within a narrow forward cone because of the limitation on transverse momentum. Hence it is justified to say that the collision occurs at a specific impact parameter b, Fig. 4.4.1 shows the essence of this approach. This is the so-called geometric picture. We therefore imagine the target to be a "tube" of area d^2b. For each b (the rest of the nucleus being spectators), the inelastic cross-section is given by

$$d\sigma_i = d^2b\,(1 - e^{-\sigma t(b)}) \qquad (4.9)$$

where the reaction probability has been written in the usual shadowing form, and σ is the inelastic hadron-nucleon cross-section.

For each b, the nuclear thickness t(b) is

$$t(b) = \int_{-\infty}^{\infty} dz\, \rho(\sqrt{b^2 + z^2}) \qquad (4.10)$$

where the nuclear density ρ is taken to be of Wood-Saxon form.

Eq. (4.9), when integrated over the entire nucleus, is of course familiar:

$$\sigma_i^{hA} = \int d\sigma_i = \int d^2b\,(1 - e^{-\sigma t(b)})$$

If one applies Eq. (3.1) to a target 'nucleus' in the

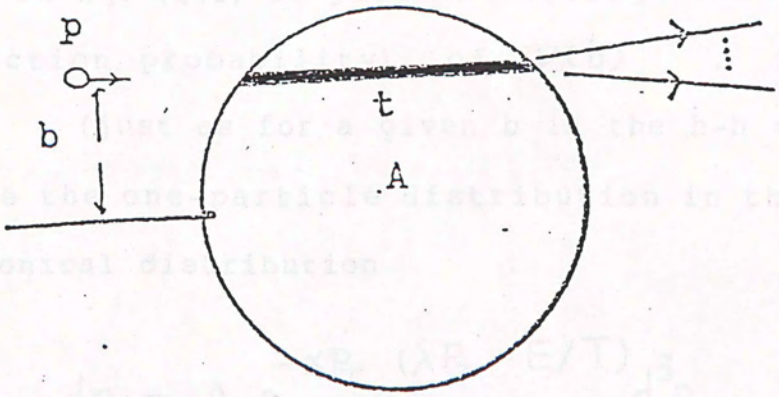

Fig. 4.4.1 Geometric picture for p-A collision.

form of a tube of area d^2b and hence mass number $A' = d^2b\, t(b)$,

$$\nu(b) = \langle \nu \rangle_{A'} = \frac{\sigma t(b)}{1 - e^{-\sigma t(b)}} \tag{4.11}$$

and $\langle \nu \rangle_A$ in Eq. (3.1) is just the average (weighted by the interaction probability) of $\nu(b)$. For a given $\langle \nu \rangle_A$ (just as for a given b in the h-h case), we parametrize the one-particle distribution in the lab frame by a canonical distribution

$$dn = A\, e^{-\alpha p_T} e^{(\lambda p_z - E/T)} \frac{d^3p}{E}$$

$$\equiv A e^{-\alpha p_T} F\, d^3p/E \tag{4.12}$$

This formula is the same as Eq. (4.8), except for the new exponential factor $e^{\lambda p_z}$, which can be understood in two ways. In p-p scattering in the centre-of-mass frame, momentum conservation is easily ensured by requiring symmetry of the one- particle distribution about $p_z = 0$. However, for h-A scattering in the lab frame, momentum conservation must be explicitly enforced through a delta function in the microcannonical ensemble. The one-particle distribution in the canonical ensemble is obtained by seeking the maximum likelihood or 'entropy' $S = \int F \ln F\, d^3p/E$, under the constraint imposed by the

delta functions; each constraint then leads to a Lagrange multiplier: $1/T$ for the conservation of energy, λ for the conservation of momentum.

Alternatively, in the centre of mass frame (with quantities denoted by *) the distribution contains only the energy Boltzmann factor $\exp(-E^*/T^*)$. Transform to the lab frame with a velocity β:

$$E^* = \gamma(E - \beta P_z) \quad , \quad \gamma = (1-\beta^2)^{-1/2}$$

then the Boltzmann factor becomes that in Eq. (4.12), with the identification

$$\frac{1}{T} = \frac{\gamma}{T^*} \quad , \quad \lambda = \frac{\gamma\beta}{T^*} \tag{4.13}$$

In fact one important aspect of our work is precisely the elucidation of what constitutes the centre of mass.

As usual, we assume the produced particles to be pions. In addition, since the data were obtained with a cut-off of $\beta > 0.85$ for the produced particles (Elias et al., 1980; Halliwell et al., 1977), the same cut-off was imposed in the numerical evaluation of $dn/d\eta$,

$$\frac{dn}{d\eta} = \int dn\, \delta(\eta - f(\theta)) \tag{4.14}$$

Of the four parameters A, α, λ, T in Eq. (4.14), we take λ to be 4.2 Gev^{-1}, so that the overall average $\langle P_T \rangle$ in the range $|y_{cm}| < 1.5$ agrees with the experimental value 0.366 Gev (Demarzo, 1984a), where the

rapidity y_{cm} is calculated in a 'centre of mass frame' assuming the target to be a single nucleon. The normalization constant A is determined by the known multiplicity η . The other parameters λ and T are used to fit the measured h-A one-particle pseudo-rapidity distribution for $\langle \nu \rangle_A = 1 - 4$ and incident energies E_o = 50, 100, 200 Gev (Elias et al., 1980; Halliwell et al., 1977). The fits are good, as shown in Fig. 4.4.2 and the values of the parameters are given in Table 4.4.1.

Table 4.4.1 Parameters for h-A collision at 50, 100, and 200 GeV incident energy, in GeV units.

ν	T	λ	A	b	γ	M
			50 GeV			
1	0.155	6.27	7.20	0.776	6.32	0.50
2	0.172	5.58	14.54	0.470	3.57	0.98
3	0.235	3.95	21.33	0.544	2.68	2.11
4	0.293	3.00	30.14	0.574	2.10	3.95
			100 GeV			
1	0.110	9.03	8.84	0.578	8.35	0.42
2	0.188	5.20	12.77	0.462	4.75	1.06
3	0.320	3.00	15.66	0.580	3.57	2.42
4	0.305	3.03	26.77	0.459	2.62	3.76
			200 GeV			
1	0.1246	7.994	6.80	0.634	12.51	0.41
2	0.200	4.96	10.64	0.678	8.13	1.04
3	0.400	2.44	13.77	0.570	4.59	2.8
4	0.290	3.3	24.60	0.372	3.45	3.34

When the incident hadron strikes a nucleus, the situation (in contrast to p-p scattering) is clearly asymmetrical and one might ask to what extent is the asymmetry 'remembered' in the final state, other than by

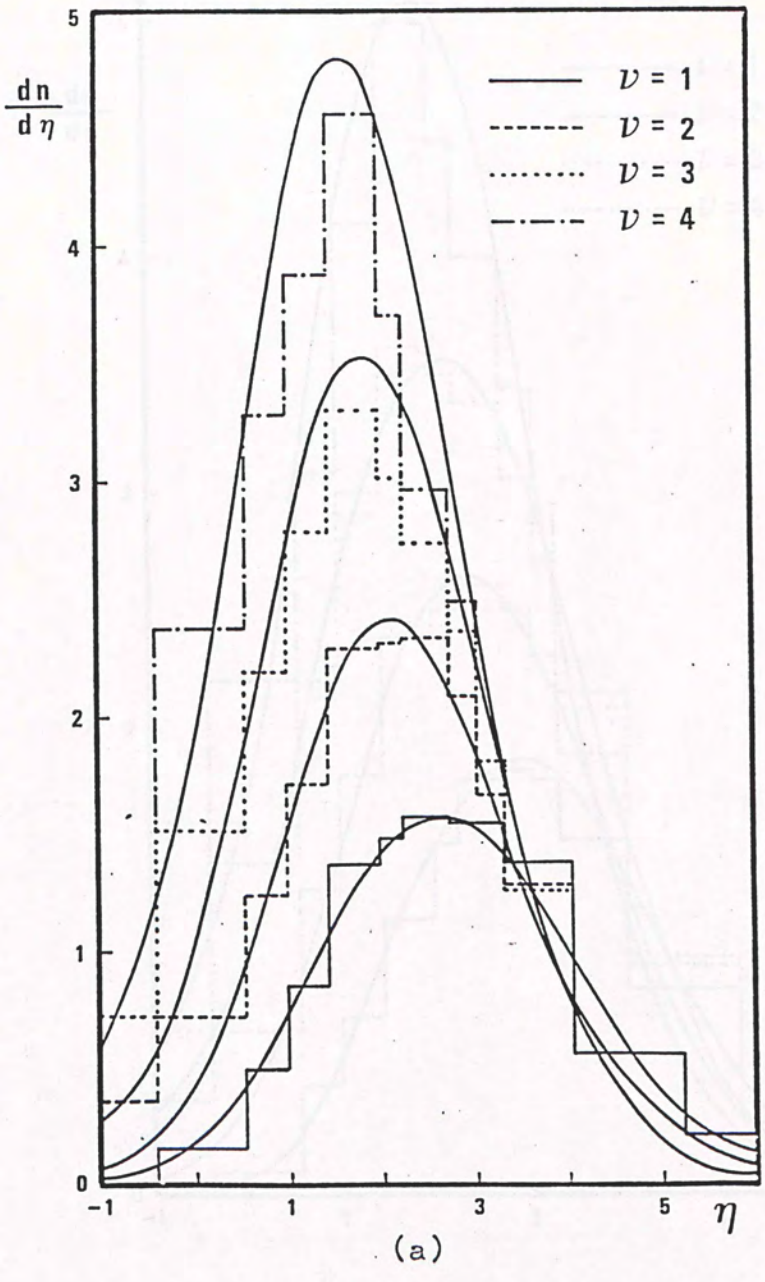

Fig. 4.4.2 The calculated differential multiplicities for h-A collisions at various incident energies: (a) 50, (b) 100 and (c) 200 GeV vs the pseudo-rapidity for different values of ν.
The corresponding data of Eilas (1980) and Halliwell (1977) are also shown.

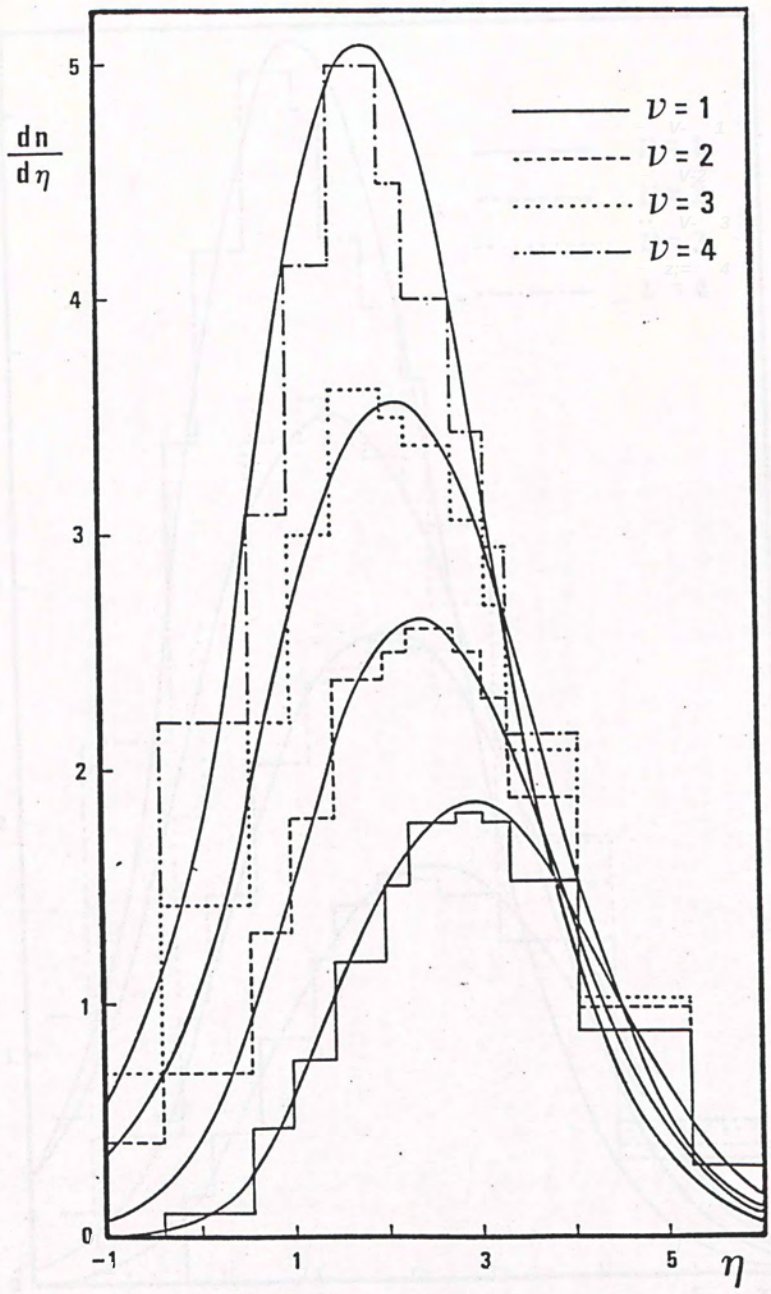

(b)

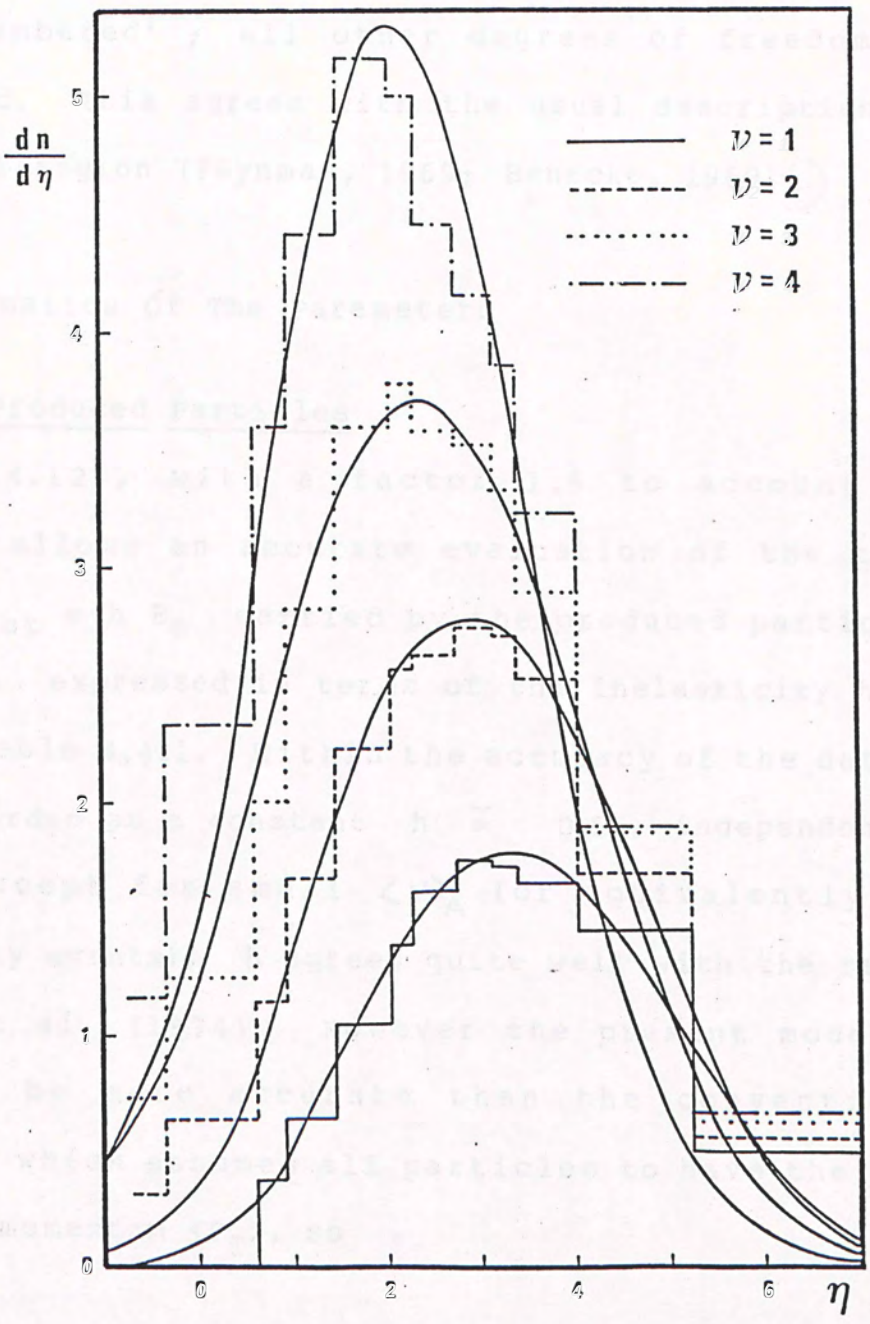

(c)

the leading particles. The success of the present model shows that for the central region, the only surviving asymmetry lies only in the total momentum. In other words, only these quantities which have to be conserved are 'remembered' ; all other degrees of freedom are thermalized. This agrees with the usual descriptions of the central region (Feynman, 1969; Benecke, 1969).

4.4.2 Systematics Of The Parameters

Energy In Produced Particles

Eq. (4.12), with a factor 1.5 to account for neutrals, allows an accurate evaluation of the total energy $E_{tot} = h\, E_o$ carried by the produced particles. The result, expressed in terms of the inelasticity h, is shown in Table 4.4.1. Within the accuracy of the data, h can be regarded as a constant $h \tilde{=} 0.56$, independent of or E_o. Except for small $\langle \nu \rangle_A$ (or equivalently low multiplicity events), h agrees quite well with the result of Jain et al. (1974). However the present model is likely to be more accurate than the conventional treatment, which assumes all particles to have the same transverse momentum $\langle P_T \rangle$, so

$$hE_o = \frac{3}{2} \langle P_T \rangle \sum_i \frac{1}{\sin\theta_i}$$

As pointed out by Chou, Yang and Yen (1985), such a definition has always involved great uncertainties, because for small θ (large η) a single emitted

particle can contribute a very large energy and it is not clear whether one should consider such particles as leading or not. Moreover, it neglects correlation between $\langle P_T \rangle$ and rapidty (Fong, 1976; Kafka, 1977).

Momentum In Produced Particles

In the same way as h, the total momentum P_{tot} carried by the produced particles in the z direction can also be evaluated from Eq. (4.12). The result is most conveniently expressed in terms of the velocity $\beta = P_{tot} / E_{tot}$ of the centre of mass of produced particles, which can be obtained directly from λ and T using Eq. (4.13). And the result is best expressed in terms of $\gamma = (1-\beta^2)^{-1/2}$ and is shown in Table 4.4.1 .

Mass Of The Target

In an h-A collision, it is generally assumed that only a part of the nucleus participates actively as an effective target, while the rest of the nucleus are spectators, with negligible momentum exchange between the two. Many dynamical models, e.g. tube models (Meng, 1977; Berlad et al., 1976), are based on untested assumptions about the nature of the effective target. We have here a complete and reasonably accurate description of the final state, which allows us to work backwards to determine the mass M of the effective target. The initial energy of the

colliding system in the lab frame is $E_o + M$, of which $(1-h)E_o$ is carried away by leading particles, so the final state should have a total energy

$$E_{tot} = E_o + M - (1-h)E_o$$
$$= hE_o + M$$

Similarly, of the incident momentum E_o, $(1-h)E_o$ is carried away by the leading particles (which are highly relativistic), so $P_{tot} = hE_o$. Hence

$$\beta = \frac{hE_o}{hE_o + M}$$

Since β can be calculated from λ and h is known, this allows us to evaluate M. The values of M are shown in Table 4.4.1 .

An implicit assumption in such an analysis is that M depends only on $\langle \nu \rangle_A$, but not on E_o (i.e. it is purely a target property) and this is indeed the case. The variation of M is shown in Fig. 4.4.3 . Although the result for M is by no means accurate, it is already sufficient to rule out the effective target being:

(1) A single nucleon ($M \sim 1$), or

(2) The whole nucleus ($M \sim A$)

In fact, the result lends support to the tube models, for which $M \sim \nu$ (Meng, 1977; Berlad, 1976).

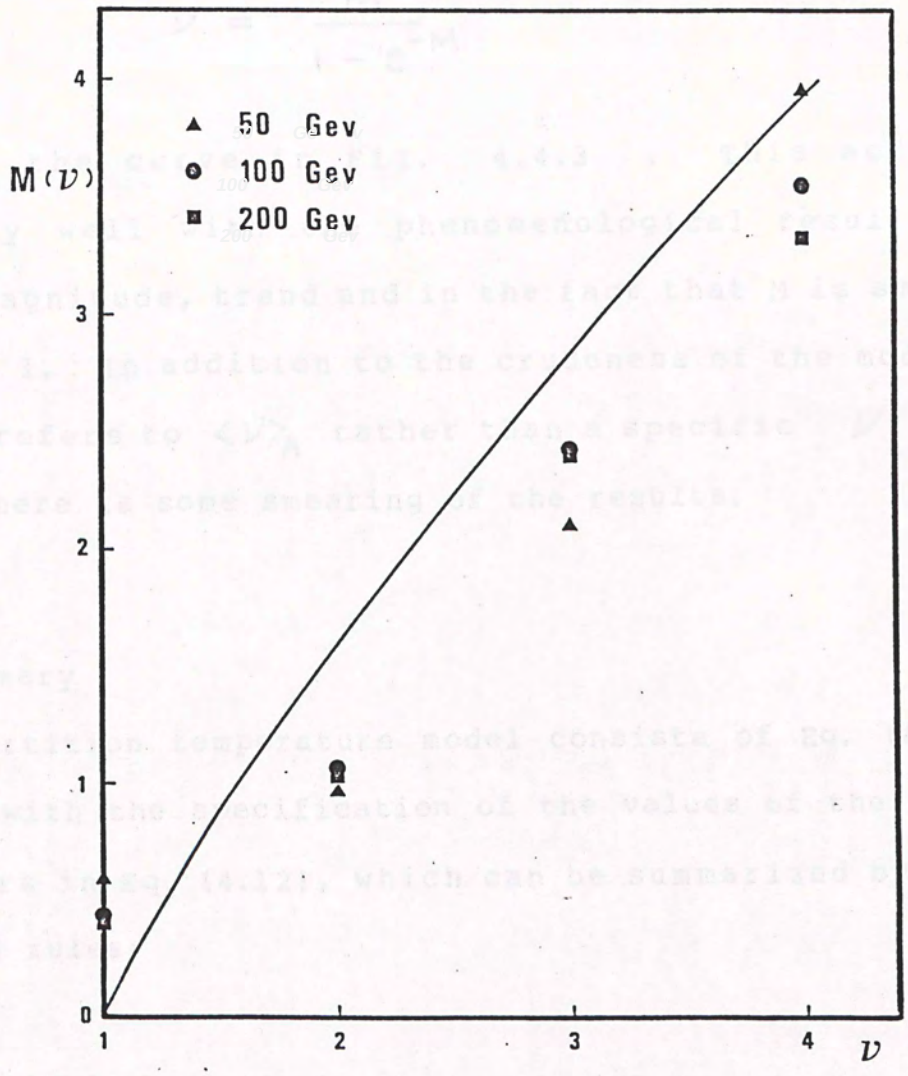

Fig. 4.4.3 Mass of the effective target M vs ν from data at 50 GeV , 100 GeV, 200 GeV . The curve $\nu = M/(1-\exp(-M))$ is also shown.

To be more specific, when a hadron of cross-section σ hits a tube of thickness t, the target mass is $M = \sigma t$ (in nucleon mass) so from Eq. (4.11)

$$\nu = \frac{M}{1 - e^{-M}}$$

which is the curve in Fig. 4.4.3 . This agrees reasonably well with the phenomenological result in overall magnitude, trend and in the fact that M is small for $\nu = 1$. In addition to the crudeness of the model, the data refers to $\langle \nu \rangle_A$ rather than a specific ν , so that there is some smearing of the results.

4.4.3 Summary

The partition temperature model consists of Eq. (4.12) together with the specification of the values of the four parameters in Eq. (4.12), which can be summarized by the following rules:

Rule 1

The normalization constant A is specified by the multiplicity, which is known to have the empirical relation Eq. (3.4), with $\beta = 0.5$, i.e. $n = n_o (1 + \nu)/2$, where is the multiplicity of h-h collision at the same energy.

Rule 2

The value of α is specified by $\langle P_T \rangle = 0.366$ Gev

Rule 3

The value of T is related to the average energy per particle, and with n known, to the total energy in produced particles. This is completely specified by h = 0.56 .

Rule 4

The value of λ is related to the mean momentum of the produced particles, which is in turn specified by stating the effective target mass M.

These four rules completely determine the single-particle distribution. Note that of the parameters in the above rules, only n_o depends on energy, roughly as (Thomé , 1977)

$$n_o = 1.20 + 0.59 \ln E + 0.12 (\ln E)^2 ,$$

with E in GeV. This provides the basis for predicting the distribution at other energies.

In short, we arrive at the following picture of h-A scattering. The incident hadron collides with a target of ν nucleons, 0.44 of the incident energy is carried away by leading particles, and the rest of energy is partitioned 'thermodynamically' among $n_o (1 + \nu)/2$ produced particles with a transverse momentum cut-off of

about 0.37 Gev/c.

4.4.4 Predictions

As a test of the four rules stated in the above section, we have used them (rather than fitted values of A, λ , T and α) to calculate, now without free parameters, the rapidity (as opposed to pseudo-rapidity) distribution, $(dn/dy)_{hA}$ for the experimentally measured one-particle distribution for Ar and Xe targets (DeMarzo et al., 1984). The input values of ν for Ar and Xe are respectively 2.3 and 3.3, which were calculated through Eq. (3.1) ; all other parameters are then determined, by the four rules stated, i.e. T = 0.251, 0.344 Gev and λ is determined from the target mass M interpolated from Table 4.4.1 . The agreement in Fig. 4.4.4 is seen to be reasonable.

The present model places much emphasis on the parameter ν and it is useful to check the dependence of the prediction. The average $\bar{R}$ of the ratio of rapidity distributions of produced particles:

$$R(y) = (dn/dy)_{pA} / (dn/dy)_{pp}$$

has been measured for Ne, Ar and Xe over three different rapidity intervals, namely :

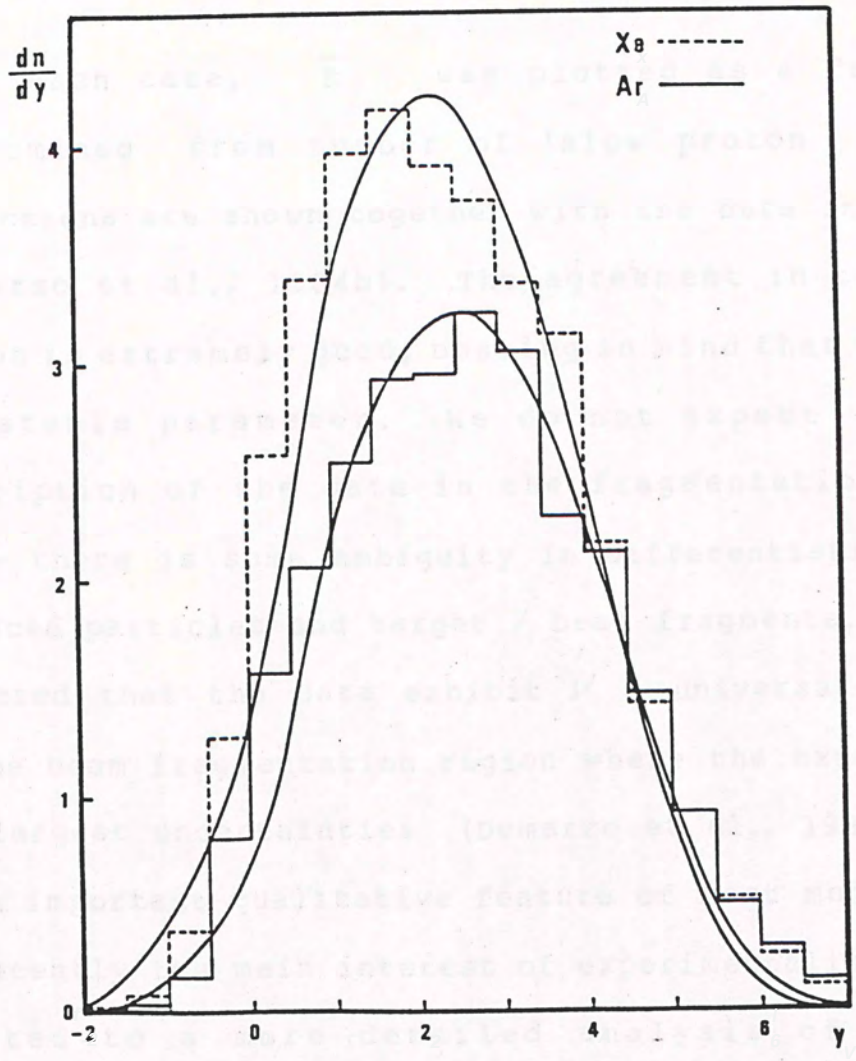

Fig. 4.4.4 The predicted rapidity distribution dn/dy from the four rules in pAr and pXe reactions. The corresponding experimental data of DeMarzo (1982) are also shown.

(1) Target fragmentation region $y < 2.0$

(2) Cental region $2.4 < y < 3.6$

(3) Beam fragmentation region $y > 5.0$

In each case, $\overline{R}$ was plotted as a function of (determined from number of 'slow proton N_p'). Our predictions are shown together with the data in Fig. 4.4.5 (DeMarzo et al., 1984b). The agreement in the central region is extremely good, bearing in mind that there is no adjustable parameter. We do not expect as good a description of the data in the fragmentation regions, where there is some ambiguity in differentiating between produced particles and target / beam fragments. It should be noted that the data exhibit ν - universality (except in the beam fragmentation region where the experiment has the largest uncertainties (Demarzo et al., 1984b)), which is an important qualitative feature of most models.

Recently the main interest of experimentalists has been devoted to a more detailed analysis of inclusive distributions. There exists a substantial amount of experimental datas on two-particle rapidity correlation in h-A interactions (Baroni, 1976; Baroni, 1978 and Gulamov, 1977).

The correlation analysis makes use of the inclusive correlation functions:

$$C(\eta_1,\eta_2) = \frac{1}{\sigma}\frac{d^2\sigma}{d\eta_1 d\eta_2} - \frac{1}{\sigma^2}\frac{d\sigma}{d\eta_1}\frac{d\sigma}{d\eta_2}$$

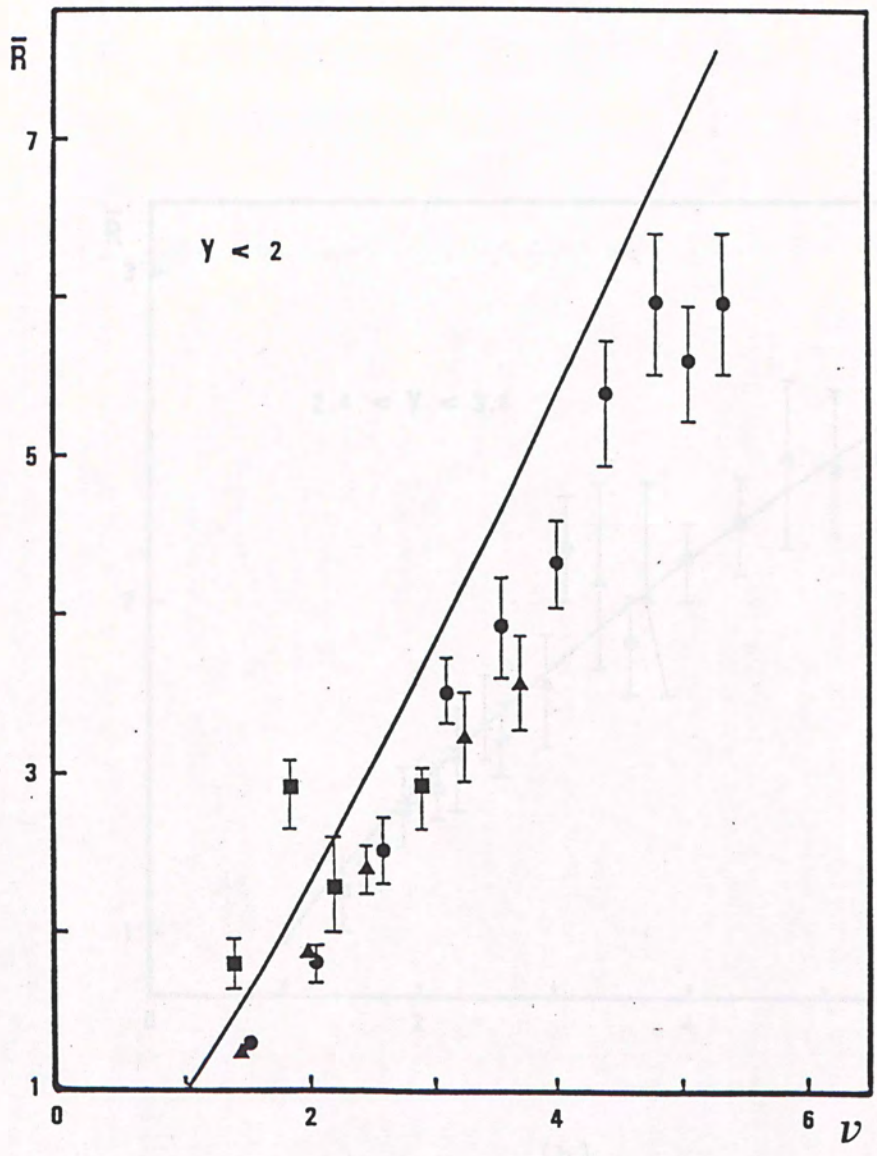

(a)

Fig. 4.4.5 The predicted average ratio $\bar{R}$ in three region (a) $y < 2$, (b) $2.4 < y < 3.6$, (c) $y > 5$ as a function of ν . Data from DeMarzo (1984b), ● Xe, ▲ Ar, ■ Ne.

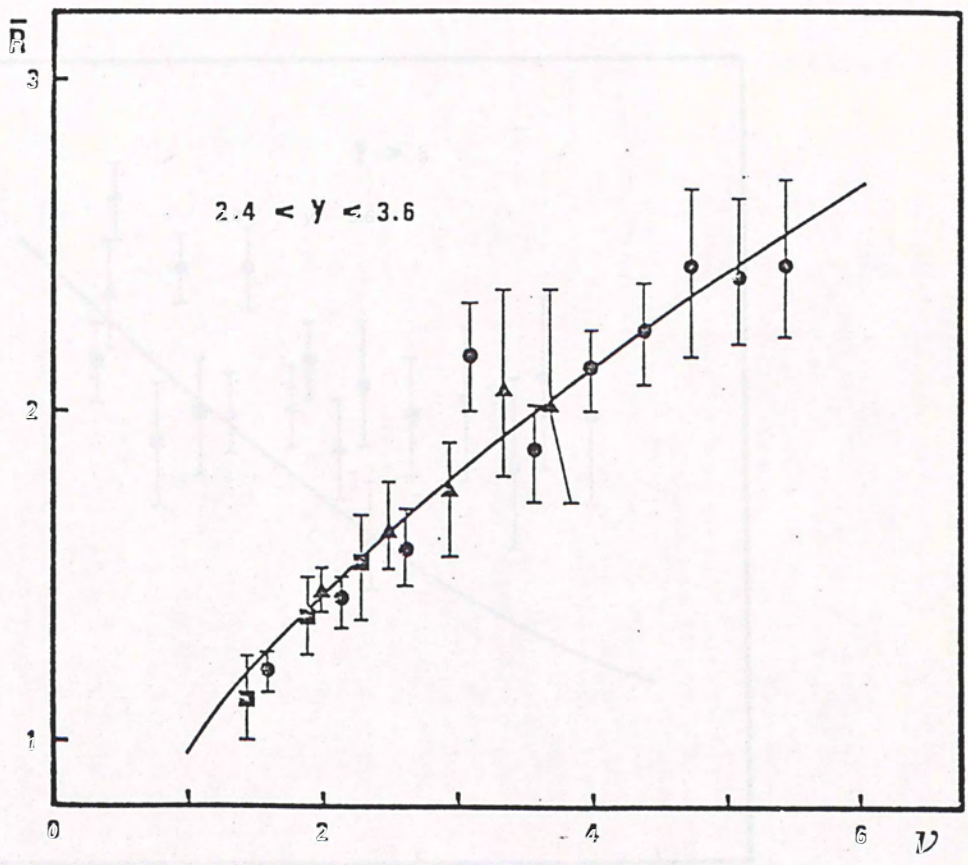

(b)

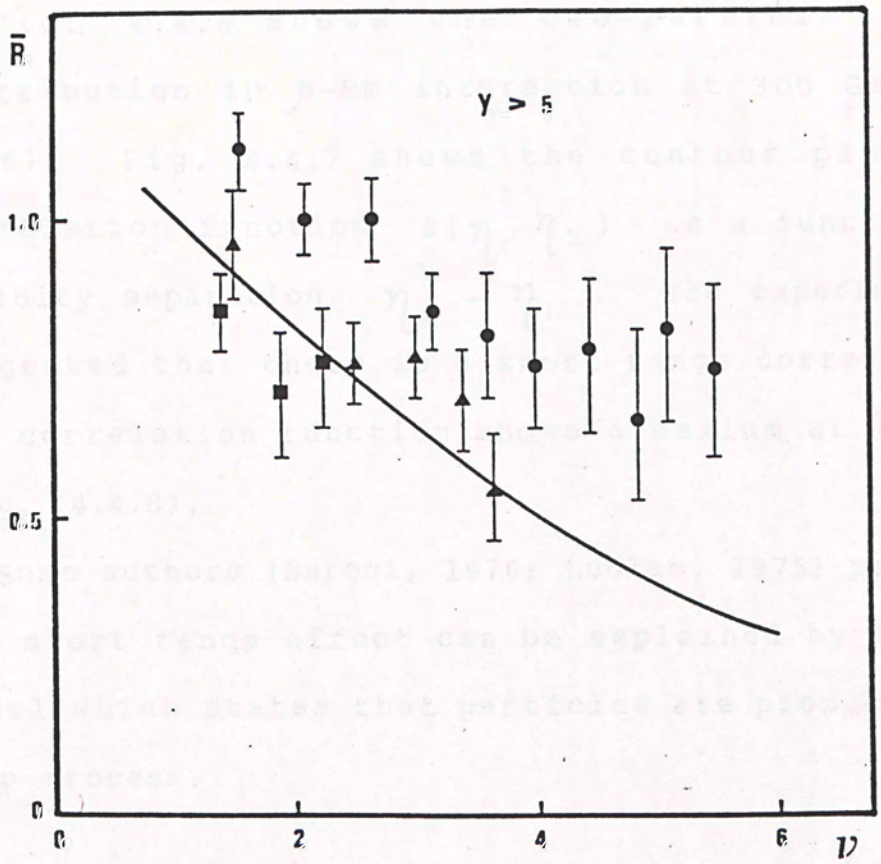

(c)

$$R(\eta_1, \eta_2) = \frac{C(\eta_1, \eta_2)}{\frac{1}{\sigma^2}\frac{d\sigma}{d\eta_1}\frac{d\sigma}{d\eta_2}}$$

where σ , $d\sigma/d\eta$ and $d^2\sigma/d\eta_1 d\eta_2$ are the inelastic cross-section, the single- and two-particle inclusive distributions, repectively.

Fig. 4.4.6 shows the two-particle inclusive distribution in p-Em interaction at 300 GeV (Baroni, 1976); Fig. 4.4.7 shows the contour plots of the correlation function $R(\eta_1, \eta_2)$ as a function of the rapidity separation $\eta_2 - \eta_1$. The experimental data suggested that there is a short range correlation, i.e. the correlation function shows a maxium at $\eta_2 - \eta_1 \cong 0$ (Fig. 4.4.8).

Some authors (Baroni, 1976; Ludlam, 1975) proposed that the short range effect can be explained by the cluster model which states that particles are produced in a two step process:

(1) production of clusters,

(2) the clusters decay into final state particles.

Our model can be applied to two-particle correlation with the following framework:

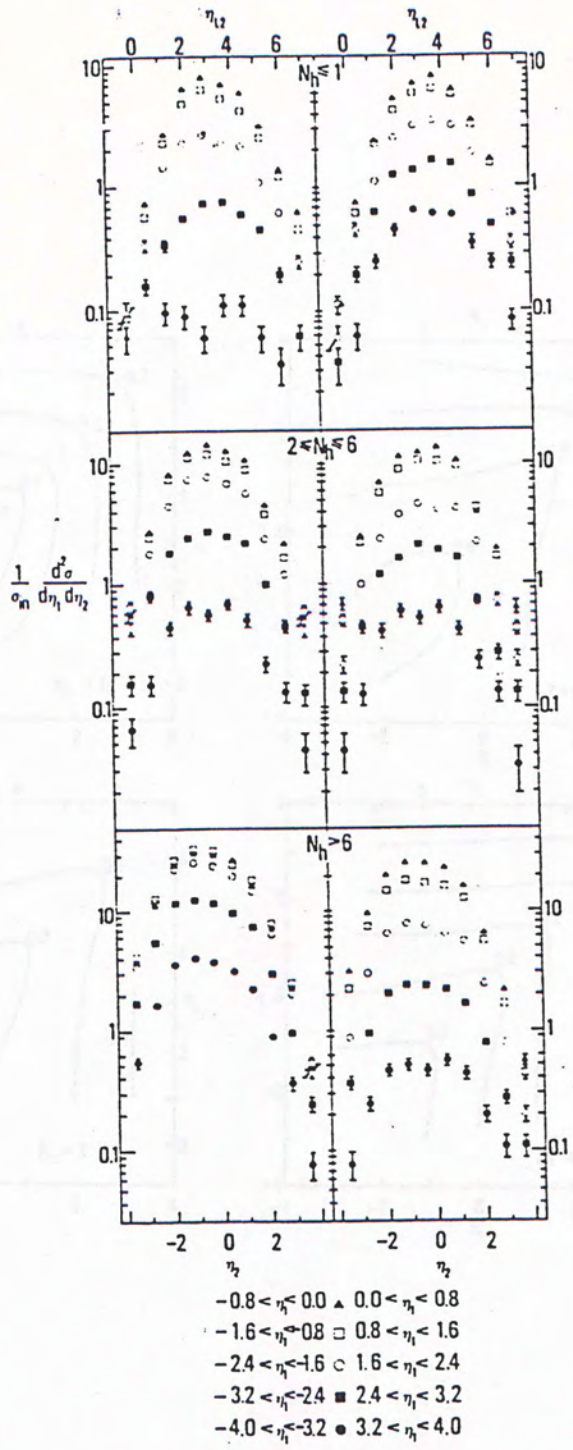

Fig. 4.4.6 Two-particle inclusive distributions in the c.m. backward (left) and forward (right) hemispheres. Taken from Baroni (1976).

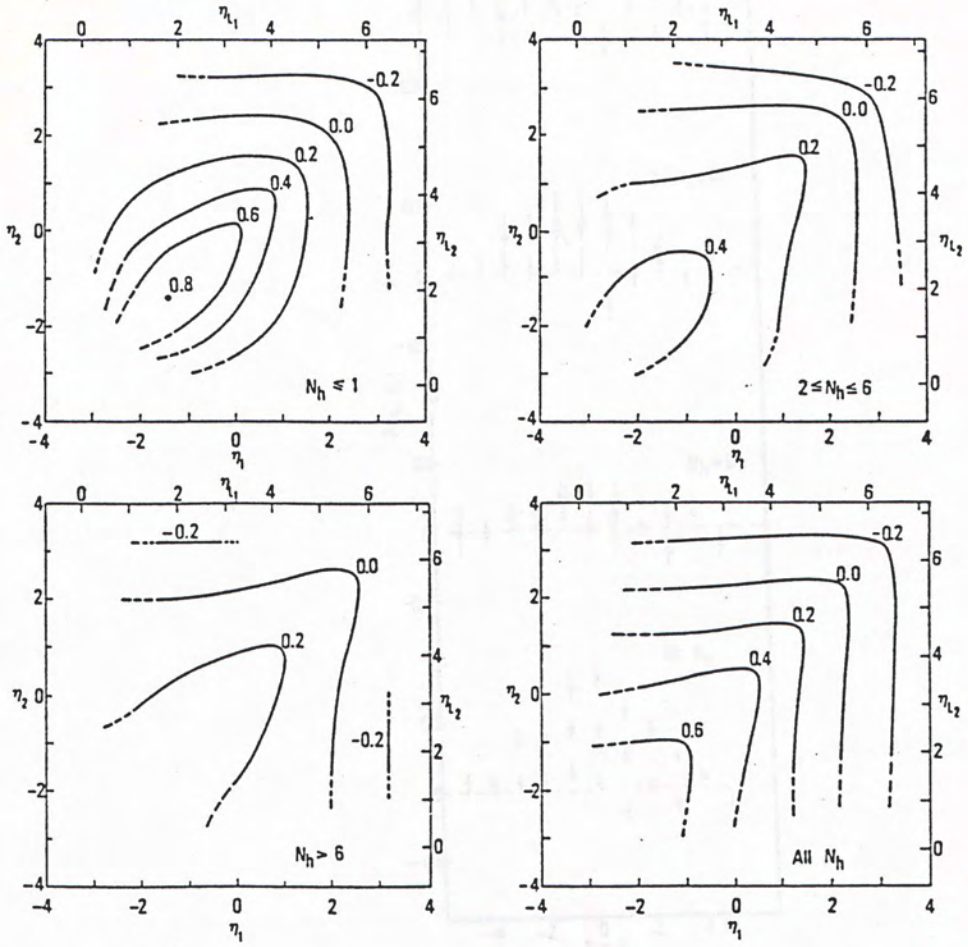

Fig. 4.4.7 Contour plots of the correlation function $R(\eta_1, \eta_2)$. Taken from Baroni (1976).

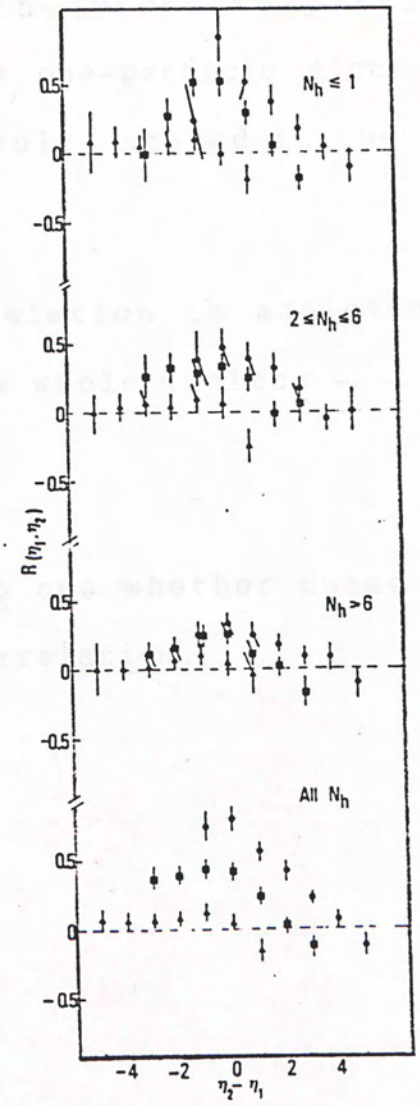

Fig. 4.4.8 Correlation function $R(\eta_1, \eta_2)$ as a function of rapidity separation $\eta_2 - \eta_1$ for different values of η_1: • =-2, ■ =0, ▲ =2. Taken from Baroni (1976).

(1) At each b, the produced particles are uncorrelated and the one-particle distribution is given by the four rules stated in the preceding sections.

(2) Rapidity correlation is achieved when we intergrate over the whole nucleus ---- sampling different b.

It would be interesting to see whether these ideas can explain the two-particle correlation.

Chapter 5

Discussion

5.1 Introduction

An important feature of the one-particle pseudo-rapidity distribution is the so-called cross-over effect: whereas $dn/d\eta$ increases with ν for small ν, it decreases with ν in the forward region. Equivalently $R_\nu(\eta) = (dn/d\eta)_\nu / (dn/d\eta)_1$ is less than unity in the forward region. We have explained this as a simple kinematic effect: as ν increases, the velocity of the centre of mass

$$\beta \sim 1 - \frac{M(\nu)}{hE_0} \sim 1 - \frac{\nu}{hE_0}$$

is smaller and as a consequence $dn/d\eta$ shifts to smaller η. This kinematic feature is implicit in several dynamical models and is responsible for their success, as summmarized below.

5.2 Multiple Scattering Model

Capella and Krzywicki (1978) proposed that in h-A collisions the state of the incident hadron may be regarded as a quantum superposition of virtual many-parton states, and in the laboratory reference frame, only slow virtual partons interact directly with the target. Each

such interaction perturbs the projectile and excites faster partons. Eventually the perturbed projectile turns into the physical multi-hadron state.

The projectile is assumed to have n independent h-N subcollisions. Moreover these subcollisions are assumed to happen as in free space, i.e. the particle produced in each h-N collision do not cascade inside the nucleus. The basic formula for the model is

$$\frac{dn}{d\eta}^{hA}(E_0, \eta) = \sum_{i=1}^{n} \frac{dn}{d\eta}^{hN}(E_i)$$

where E_0 is the incident energy and E_i is the h-N subcollision energy. It is further assumed that the energy E_0 is equally distributed among the n subcollisions, i.e. $E_i = E_0 / n$ for all i. The distribution of produced particles from each subcollision is centred about the centre of mass rapidity defined by E_0 / n hitting one nucleon. The centre-of-mass rapidty is obviously the same as that defined by the total energy E_0 hitting n nucleons.

$$y_{cm} = \text{arctanh}\left(\frac{E_0/n}{E_0/n + 1}\right) = \text{arctanh}\left(\frac{E_0}{E_0 + n}\right)$$

The number n is identified with ν , at least in an average sense, so the kinematics corresponds precisely to our conclusion $M(\nu) \sim \nu$. The predictions of the model is shown in Fig. 5.2.1 ; they seem to describe the experimental data well. We emphasize

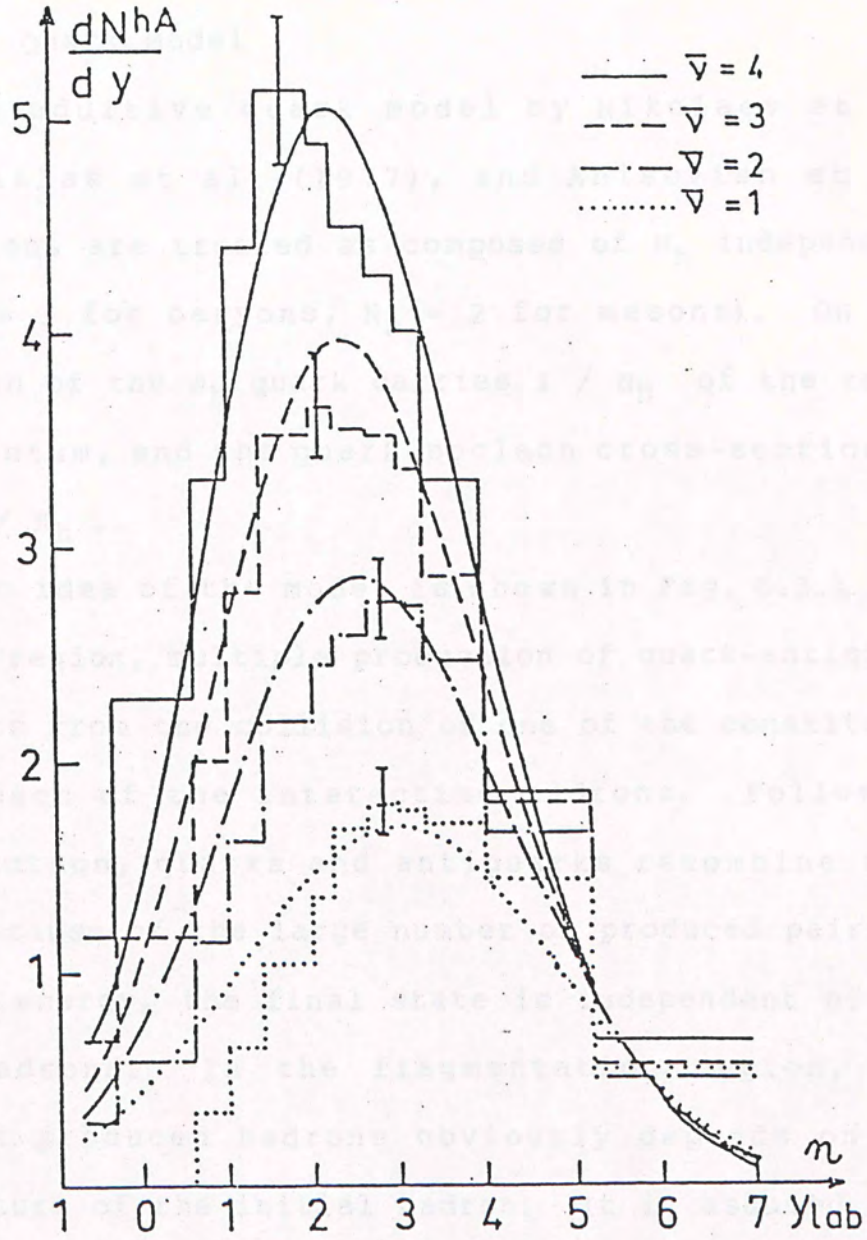

Fig. 5.2.1 The predicted pseudo-rapidity distribution dn/dη from the multiple scattering model. The corresponding data of Eilas (1980) is also shown. Taken from Capella (1978).

that the success is mainly due to the incorporation of the right kinematics.

5.3 Additive Quark Model

In the additive quark model by Nikolaev et al. (1978), Bialas et al. (1977), and Anisovish et al. (1978), hadrons are treated as composed of N_h independent quarks (N_h = 3 for baryons, N_h = 2 for mesons). On the average, each of the N_h quark carries 1 / N_h of the total hadron momentum, and the quark-nucleon cross-section is σ_{hadron} / N_h.

The basic idea of the model is shown in Fig. 5.3.1 . In the central region, multiple production of quark-antiquark pairs results from the collision of one of the constituent quarks of each of the interacting hadrons. Following their production, quarks and antiquarks recombine into hadrons. Because of the large number of produced pairs at high enough energy, the final state is independent of the incident hadrons. In the fragmentation region, the spectrum of produced hadrons obviously depends on the quark structure of the initial hadron. It is assumed that one of the quarks or antiquarks of the initial hadron was lost in the collision, thus giving rise to the central production. The remaining spectator quark from a meson (or a diquark from a baryon) has continued its flight with unchanged momentum and may recombine with centrally produced quark or antiquark to form a final-state hadron.

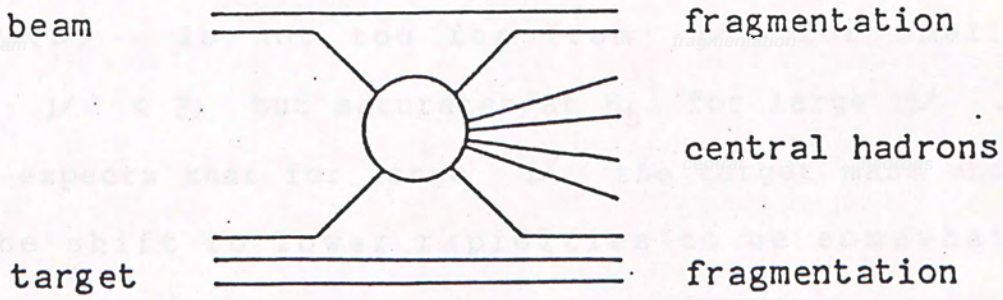

Fig. 5.3.1 Illustration of the basic idea of additive quark model. Taken from Kittel (1981).

Each of the constituent quarks can collide with a target nucleon and then becomes a "wounded" quark which cannot collide again. For a reaction with ν target nucleons, there will be $W(\nu)$ quark-nucleon collisions, where it is assumed that.

$$W(\nu) = N_h \left[1 - \left(1 - \frac{1}{N_h} \right)^{\nu} \right] \qquad (5.1)$$

So the target mass would be $M \sim W(\nu)$. And based on Eq. (5.1) $W(\nu)$ is not too far from ν for small ν (say $\nu < 3$) but saturates at N_h for large ν. Thus one expects that for large ν the target mass and hence the shift to lower rapidities to be somewhat underestimated. However this is compensated by the assumption that the low energy portion of the produced particles rescatter, yielding more particles at low rapidities. Furthermore, one is unable to sample very large ν, where the greatest difference will show up. Thus the model agrees fairly well with the measured one-particle distribution (Demarzo, 1984b). Fig. 5.3.2 shows the experimental data and predictions of the model.

5.4 Conclusion

There are of course a number of other models which fit the one-particle distribution with varying degrees of success. Our work shows that the correct kinematics (e.g. $M(\nu) \sim \nu$; energy conservation translated into a

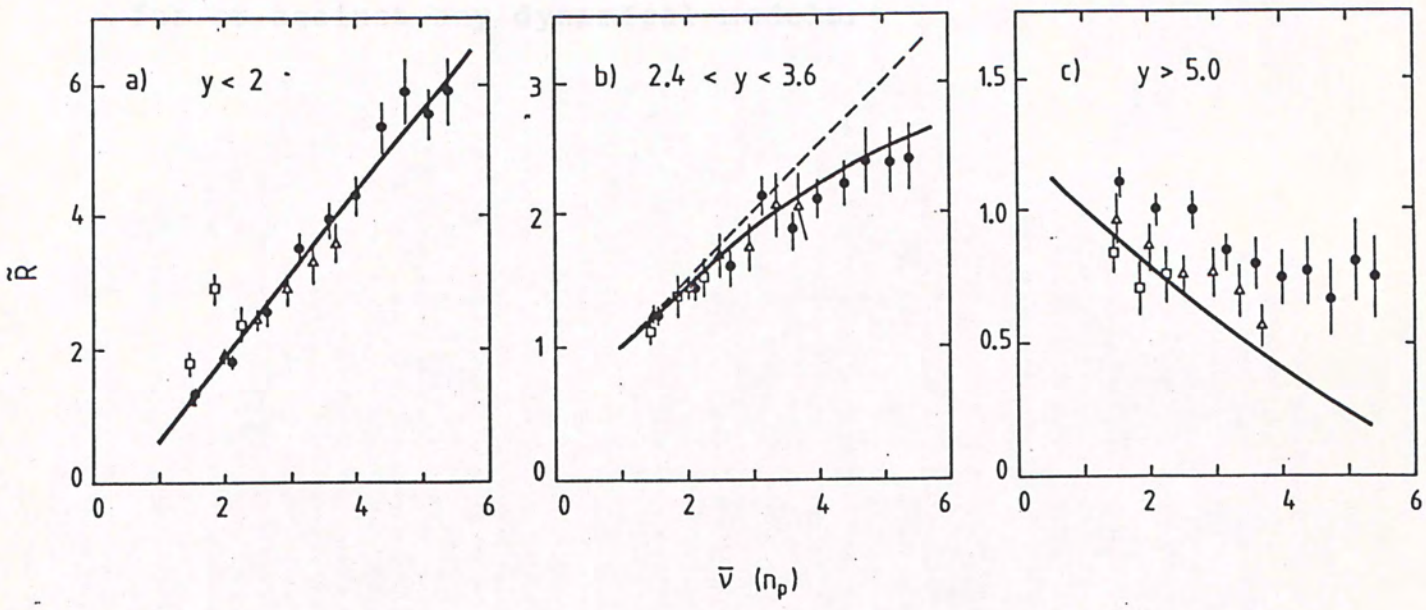

Fig. 5.3.2 The predicted average ratio R from additive quark model compared with experiment. Taken from DeMarzo (1984b).

partition temperature) plus ignorance about the dynamics ('ignorance' being manifested as the maximization of 'entropy') is already adequate to account for the data. Therefore the one - particle distribution, especially in the cental region, is unlikely to provide decisive tests for or against any dynamical models.

References

Alkhazov, G. D. et al., 1976, Nucl. Phys. A274, 443.

Anderson, R. L. et al., 1970, Phys. Rev. Lett. 25, 1218

Andersson, B., I. Otterlund and E. Stenlund, 1978, Phys. Lett. 73B, 343.

Anisovish, V. V., Yu. M. Shabelsky and V. M. Shekhter, 1978, Nucl. Phys. B135, 477.

Antinucci, M. et al., 1973, Lett. Nuovo Cimento, 6, 21.

Anzon, Z. V. et al., 1977, Nucl. Phys. B129, 205.

Ayres, D. S. et al, 1977, Phys. Rev. D15, 3105.

Banner, M. et al., 1972, Proc. Chicago Conference.

Barash-Schmidt, N. et al., 1980, Revs. Mod. Phys. 52.

Baroni, G. et al., 1976, Nucl. Phys. B103, 213.

Baroni, G. et al., 1978, Nucl. Phys. B135, 405.

Barton, D. S. et al., 1983, Phys. Rev. D27, 2580.

Battision, R. et al., 1982, Phys. Lett. 115B, 333.

Babecki, J. et al., 1978, Acta Phys. Pol. B9, 495.

Benecke, J. et al., 1969, Phys. Rev. 188, 2159.

Berlad, G. et al., 1976, Phys. Rev. D13, 161.

Bertin, A. et al., 1972, Phys. Lett. 42B, 493.

Bialas, A., W. Czyz and W. Furmanski, 1977, Acta Phys. Pol. B8, 585.

Böhm, A. et al., 1974, Phys. Lett. 49B, 491.

Boos, E. G. et al., 1978, Nucl. Phys. B143, 232.

Busza, W., 1977, Acta Phys. Pol. B8, 333.

Busza, W., 1983, Proc. 13th Int. Symp. on Multiparticle Dynamics, 367.

Busza, W., 1984, 15th Symp. on Multiparticle Dynamics, Lund.

Carroll, A. S. et al., 1979, Phys. Lett. 80B, 319.

Capella, A. and A. Krzywicki, 1978, Phys. Rev. D18, 3357.

Capella, A. and J. Tran Thanh Van, 1980, Phys. Lett. 93B, 146.

Chao, W. Q. et al., 1983, Nucl. Phys. A395, 482.

Charpak, G., 1968, Nucl. Instrum. Meth., 62, 235.

Chikovani, G. E. et al., 1964 Nucl. Instrum. Meth., 29, 261.

Chou, T. T. and C. N. Yang, 1968, Phys. Rev. 170,1591.

Chou, T. T., C. N. Yang and E. Yen, 1985, Phys. Rev. Lett. 54, 510.

Cincheza, J. et al., 1979, Nucl. Phys. B158, 280.

Czyzewski, O., 1968, in Proc. 14th Int. Conf. on High Energy Physics (CERN).

DeMarzo, C. et al., 1982, Phys. Rev. D26, 1019.

DeMarzo, C. et al., 1984a, Phys. Rev. D29, 363.

DeMarzo, C. et al., 1984b, Phys. Rev. D29, 2476.

Detar, C. E., 1971, Phys. Rev. D3, 128.

Elias, J. E. et al., 1980, Phys. Rev. D22, 12.

Fabjan, C. W. and H. G. Fisher, 1980, Rep. Prog. Phys. 43, 1003.

Faessler, M. A. et al,. 1979, Nucl. Phys. B157, 1.

Fermi, E., 1950, Prog. Theor. Phys. 5, 570.

Feynman, R. P., 1969, Phys. Rev. Lett. 23, 1415.

Fong, D. et al., 1976, Phys. Lett. 61B, 99.

Frisch, H. J. et al., 1983, Phys. Rev. D27, 1001.

Giacomelli, G. 1972, Proceedings of the Sixteenth International Conference on High Energy Physics.

Gottfried, K., 1974, Phys. Rev. Lett. 32, 957.

Gulamov, K. et al., 1977, Z. Phys. A280, 1077.

Halliwell, C. et al., 1977, Phys. Rev. Lett. 39, 1499.

Horn, D. and F. Zachariasen, 1973, Hadron Physics at Very High Energies (Benjamin Inc.).

Jain, P. L. et al., 1974, Phys. Rev. Lett. 33, 660.

Kac, M., 1973, Nucl. Phys. B62, 402.

Kafka, T. et al., 1977, Phys. Rev. D16, 1261.

Kittel, W., 1972, CERN/D. Ph. II/Phys. 72-49.

Kittel, W., 1981, Proc. Europhys. Study Conf., Erice.

Koba, Z., H. B. Nielsen and P. Olesen, 1972, Nucl. Phys. B40, 317.

Landau, L. D., 1953, Izv. Akad. Nauk SSSR, ser. fiz. 17, 51.

Li, T. S. and K. Young, 1986, Phys. Rev. D34, no. 1.

Ling, S. H. and K. Young, 1985, Can. J. Phys. 63, 954.

Ludlam, T. and R. Slansky, 1975, Phys. Rev. Lett. 35, 127

Meng, T., 1977, Phys. Rev. D29, 2476.

Milekhin, G. A., 1959, Sov. Phys. JETP, 35, 829.

Nikolaev, N. N. and A. Ya Ostapchuck, 1978, CERN Report TH 2575.

Otterlund, I. et al., 1978, Nucl. Phys. B142, 445.

Perkins, D. H., 1982, Intro. to High Energy Physics (Addison-Wesley Publishing Company Inc.).

Perl, M., 1973, High Energy Hadron Physics (John Wiley & Sons).

Pomeranchuk, I. Ya., 1951, Dokl. Akad. Nauk SSSR 78, 889.

Predazzi, E., 1979, Rivista Del Nouvo Cimento 2, 1.

Rees, C. D. et al., 1983, Z. Phys. C17, 95.

Segre, E., 1973, Nuclei and Particles (Benjamin).

Sens, J. C., 1972, Oxford Conference.

Thomé, W. et al., 1977, Nucl. Phys. B129, 365.

Whitemore, J., 1974, Phys. Rep. 10C, 237.